Three-Dimensional Evolution of Simulated Long-Lived Squall Lines

WILLIAM C. SKAMAROCK, MORRIS L. WEISMAN, AND JOSEPH B. KLEMP

National Center for Atmospheric Research, Boulder, Colorado*

(Manuscript received 17 May 1993, in final form 2 February 1994)

ABSTRACT

Simulations of squall lines, using nonhydrostatic convection-resolving models, have been limited to two dimensions or three dimensions with the assumption of along-line periodicity. The authors present 3D nonhydrostatic convection-resolving simulations, produced using an adaptive grid model, where the lines are finite in length and the restriction to along-line periodicity is removed. The base state for the simulations is characterized by weak, shallow shear and high convective available potential energy (CAPE), an environment in which long-lived midlatitude mesoscale convective systems (MCSs) are observed. The simulated systems bear strong resemblance to many observed systems, suggesting that large-scale forcing, absent in the horizontally homogeneous environment, is not needed to produce many of the distinguishing features of midlatitude MCSs.

In simulations without Coriolis forcing, the presence of line ends leads to mature symmetric systems characterized by a central region of strong convection, trailing flanks of weaker convection, and a strong, centrally focused rear inflow. Simulations that include Coriolis forcing lead to asymmetric systems with significant system growth and migration to the right (south) of the original system centerline. In both cases the evolution of the leading-line convection is primarily controlled by the surface cold pool expansion, with Coriolis forcing promoting rightward system propagation. In the Coriolis simulation, a midlevel mesoscale convective vortex (MCV) forms in the north, to the rear of the convection, while the outflow region aloft is strongly anticyclonic. The northern location of the MCV is coincident with and influenced by a northward bias in the positive buoyancy anomaly aloft. Midlevel vertical vorticity generation by tilting of horizontal vorticity, both ambient and baroclinically generated, is observed in both the Coriolis and no-Coriolis simulations. On larger scales, the convergence of Coriolis rotation generates significant vorticity and is crucial to the formation of the MCV.

1. Introduction

Observational studies of long-lived convective systems reveal a variety of mature structures, ranging from quasi-two-dimensional squall lines to fully three-dimensional mesoscale convective systems (MCSs). Theoretical and convection-resolving modeling studies of convection have concentrated on the former type of system because of the substantial simplification afforded by the two-dimensional geometry and also because of limitations in computational resources. Nonhydrostatic numerical studies that actually resolve the convection have been limited to either strictly two-dimensional domains or three-dimensional domains with a periodic constraint employed in the along-line direction. While these studies have revealed much about the dynamics of line-oriented convective systems, the inability to represent finite-extent lines and the asymmetric influences of Coriolis effects has prevented such models from replicating many of the significant three-dimensional characteristics of the long-lived systems. Such features may be important in MCSs, for which observations have revealed significant along-line variability of the convective circulation, generation of anticyclonic outflow aloft and, in some cases, generation of midlevel mesoscale convective vortices (MCVs).

In this paper we examine the more fully three-dimensional evolution of simulated convective systems by employing a nonhydrostatic adaptive-grid model in which both the convection and the larger-scale flow are resolved without the constraint of along-line periodicity. The simulated systems reproduce many features often associated with MCSs, and the completeness of the model datasets provides a more detailed picture of idealized MCS evolution from inception to maturation. We find that asymmetries characteristic of those observed in MCSs evolve naturally from finite-extent lines, particularly in the presence of the earth's rotation, and that there are significant interactions between the convective and system scales.

Detailed observations of fully three-dimensional systems have generally been limited to the systems' mature and decaying states, and there are few observations of these systems as they evolve from their inception to

---

* The National Center for Atmospheric Research is sponsored by the National Science Foundation.

Corresponding author address: Dr. William C. Skamarock, NCAR/MMM Division, P.O. Box 3000, Boulder, CO 80307-3000.

their maturity. Based on a study of heavy rain events in Oklahoma, Houze et al. (1990) identifies two types of mature structures that are characteristic of organized MCSs. The first, referred to as *symmetric* (Fig. 1a), is characterized by a traditional leading-line, trailing-stratiform region squall line. Most 2D squall line theories and modeling studies focus on lines of this type. In contrast to the 2D models, though, the line bows out at the center where cells tend to be stronger than those located near the ends. The second, referred to as *asymmetric* (Fig. 1b), exhibits strong system-scale 3D circulations, including a midlevel MCV to the rear of the northern part of the line. While the region of stratiform precipitation in such cases is located toward the northern line end, the strongest cells are often found along the southern end. Vertical cross sections through the core of these conceptual systems depict the classic mature squall line signatures: a strong front-to-rear flow extending from the convective region rearward above a surface cold pool and a rear-inflow jet that descends toward the surface as it approaches the leading edge of the system (Houze et al. 1989, Fig. 1). While Houze et al. (1989) and Houze et al. (1990) presented two conceptual models, they also identified systems spanning a wide spectrum of possible types, including many systems that displayed little mesoscale organization. Houze et al. (1990) found that systems occurring in weaker ambient wind shear tended to generate more organized mesoscale front-to-rear and rear-to-front flows as opposed to the more isolated, disorganized convective cells observed in strong-shear environments.

The term *mesoscale convective complex* (MCC) is generally applied to any of the above systems that develops a large circular cold cloud shield (as visible on an IR satellite image) that lasts for at least 6 h (Maddox 1980). Bartels and Maddox (1991) discuss three distinct mesoscale circulations consistently associated with mature MCCs: a large, cold, divergent anticyclone aloft, a cold divergent mesohigh at the surface, and midlevel convergence associated with a warm mesoscale updraft and descending rear inflow jet. Maddox (1983) found that the environmental conditions associated with the development of MCCs were quite similar to that for the organized MCSs, including a conditionally unstable air mass and generally weak vertical wind shear. The MCCs tended to develop and organize within a mesoscale region of upward vertical motion associated with strong low-level warm advection ahead of a weak midlevel trough. Maddox (1983) suggests that MCCs interact with the larger-scale environment primarily by their moistening of a deep tropospheric layer and by creating large-scale temperature perturbations associated with both the warm mesoscale updraft at midlevels and the cold outflow aloft.

The similarities in the structure and evolution of MCCs and smaller MCSs bring into question whether a dynamical distinction exists among convective systems based on scale alone. In this regard, recent attention has focused on the MCV associated with the asymmetric convective systems. MCVs are observed in MCC as well as non-MCC systems, and may range in diameter from a few tens of kilometers (e.g., Stirling and Wakimoto 1989; Verlinde and Cotton 1990) to a few hundred kilometers (e.g., Bartels and Maddox 1991). The vortex circulations are generally identifiable beginning at 1–2 km AGL and continuing up through 5–8 km, with the lifetime ranging from several hours for the smaller-scale vortices to several days for larger-scale vortices (which may significantly outlive

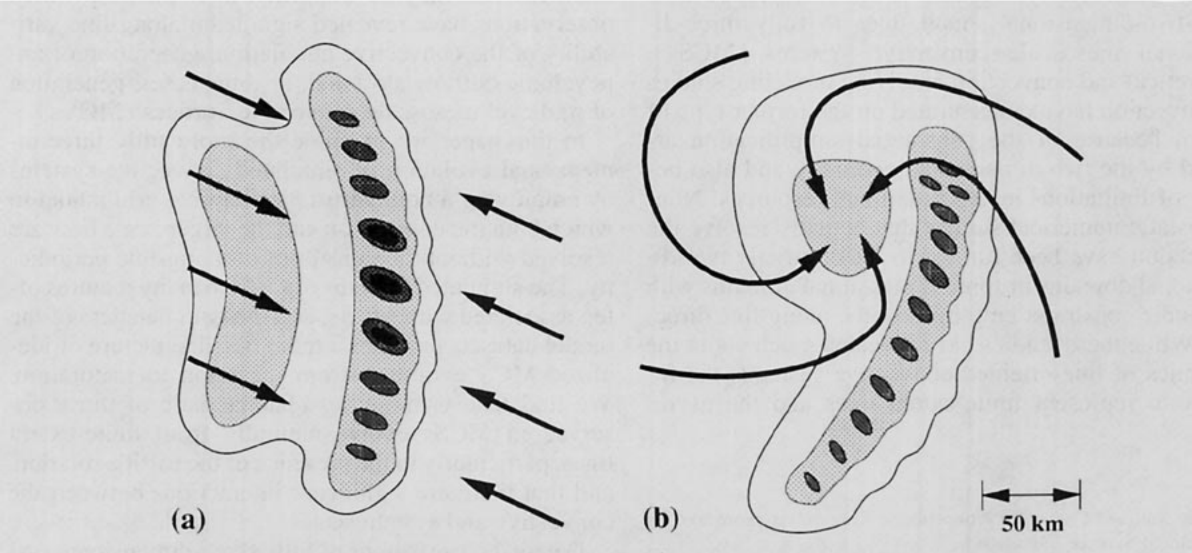

FIG. 1. Midlevel cross sections through conceptual models of (a) a symmetric leading-line trailing stratiform MCS and (b) an asymmetric MCS with a well-defined vortex. The storm-relative flow is superposed on the low-level radar reflectivity with heavier stippling denoting higher reflectivity. Adapted from Houze et al. (1989) and Houze et al. (1990).

the parent convective system). In long-lived cases, the existence of the MCV may be revealed in the midlevel cloud patterns following the decay of the upper-level anvil (e.g., Johnston 1981; Menard and Fritsch 1989). Velasco and Fritsch (1987), however, found that only 5% of MCSs contain MCVs that live long enough to be visible in this manner. Leary and Rappaport (1987) document one long-lived MCV case in which the stratiform precipitation region was organized into curved rainbands. In some instances, the MCVs have been observed to be associated with convection on subsequent days, possibly due to induced mesoscale lifting (Menard and Fritsch 1989). Bartels and Maddox (1991) find that large CAPE and weak vertical wind shear are conducive to the formation of long-lived MCVs and that strong background (relative) vorticity and strong larger-scale forcing are not needed for system development.

Considering the absence of significant background vertical vorticity, several other sources of vorticity have been postulated for the generation of the MCV. Bartels and Maddox (1991) and Johnson and Bartels (1992) find that stretching of earth's rotation associated with midlevel convergence within the stratiform precipitation region was sufficient to generate many observed MCVs. Brandes (1990) and Brandes and Ziegler (1993) found that convergence of preexisting vorticity was significant in the 6–7 May 1985 PRE-STORM MCS but also found that tilting of horizontal vorticity played a major role in the lower-level vortex strength. Biggerstaff and Houze (1991) suggest that tilting of ambient horizontal vorticity may be important in shaping the vorticity structure of the 10–11 June 1985 PRE-STORM system.

The thermodynamic structure within MCVs appears to vary considerably. Johnson and Bartels (1992) found the central region of an MCV to be warmer than its surroundings in the 23–24 June 1985 OK PRE-STORM system. In the 6–7 May 1985 Oklahoma MCS, Brandes (1990) found the surrounding environment to be warmer than the vortex core for the lower portion of the vortex and colder than the vortex core for the upper portion of the vortex. In a mesoscale modeling study of the 10–11 June 1985 PRE-STORM MCS, Zhang (1992) argues that MCVs can be induced by both heating and cooling. The vertical velocities within the MCV also vary; some MCVs are apparently located within a mesoscale updraft, while others are located within a mesoscale downdraft. While the dynamical significance of these various structures has only been speculated upon, Raymond and Jiang (1990) note that the generation of an MCV located between a warm potential temperature anomaly aloft and a cold anomaly at the surface is consistent with the existence of a positive potential vorticity anomaly at midlevels, suggesting that the interactions between the MCV, the convective system, and the larger-scale flow may be understood through potential vorticity dynamics. They have also shown that the interaction between a midlevel potential vorticity anomaly and ambient vertical wind shear can induce mesoscale motions that could enhance an existing convective system or help trigger a new convective system. The existence of a midlevel positive potential vorticity anomaly is also consistent with speculations that larger-scale MCVs are stable and that these contribute to their longevity.

Mesoscale modeling studies have had some success in simulating observed midlatitude MCSs (e.g., Zhang and Fritsch 1987, 1988a; Zhang et al. 1989), particularly those that have been strongly forced by the larger-scale conditions. The studies, focusing primarily on model predictability, reveal that both convective parameterizations and explicit "resolvable-scale" moist-diabatic processes must be included in the models to capture overall MCS evolution (Zhang and Fritsch 1988b; Zhang et al. 1988). The explicit processes are important for producing stratiform rain regions and MCVs, while the parameterized convection is crucial for simulating the size, orientation, and evolution of the MCSs. Overall, the model simulations demonstrate that simulations of MCS evolution and their accompanying rainfall are possible in at least some cases. However, while the mesoscale modeling studies have complemented observations and given insight into the evolution of the systems, conceptual models of system evolution based on the studies have not been forthcoming. This is because it is difficult to untangle the interactions among the larger-scale synoptic flow, the system-scale circulations developed by the convection, and the convective-scale motions in the real-data cases, particularly when convection is not resolved in the simulations.

Studies using 2D and 3D periodic nonhydrostatic convection-resolving models have focused on identifying the structure and evolution of the leading-line convection and the subsequent generation of the stratiform precipitation region. These studies have revealed that the evolution from a narrow convective line to a mature mesoscale convective system occurs systematically in response to the development and intensification of a convectively generated cold pool. This evolution is represented schematically in Fig. 2, which depicts a convective system growing in an environment with weak to moderate vertical wind shear. At early times, the convective cells lean downshear in response to the ambient shear (Fig. 2a). As the cold pool strengthens, however, the system changes its orientation to upright (Fig. 2b), and then finally to an upshear tilt (Fig. 2c) in response to negative horizontal vorticity generated at the leading edge of the cold pool. It is during this upshear-tilting phase that a stratiform precipitation region and a significant rear-inflow jet are generated, with the rear inflow forming in response to the horizontal buoyancy gradients that are generated at the back edge of the expanding system [associated with the warm convective plume aloft and the cold pool at

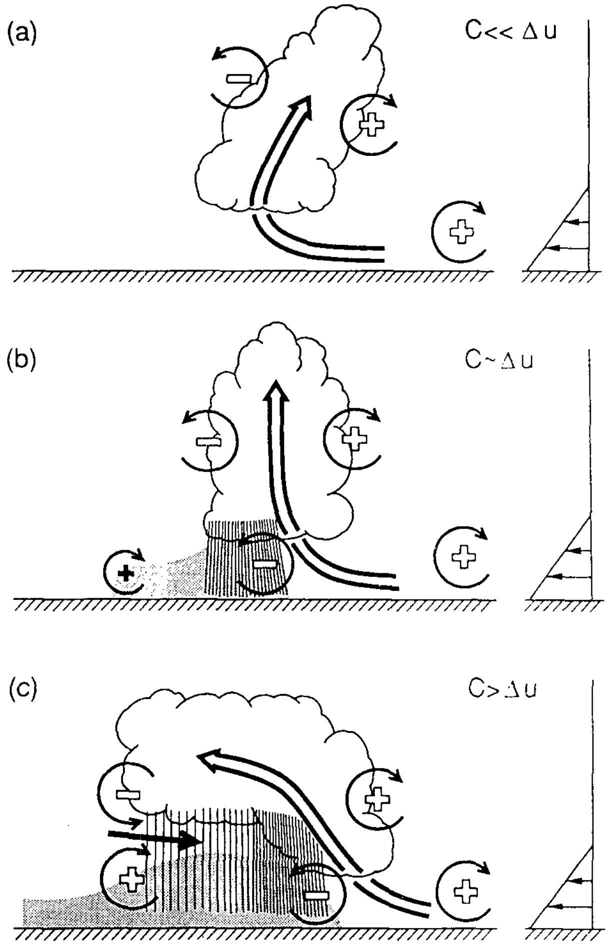

FIG. 2. Three stages in the evolution of a convective system. The system tilt evolves through a (a) downshear, (b) vertical, and (c) upshear orientation over time. From Weisman (1992).

the surface; e.g., Lafore and Moncrieff (1989); Fovell and Ogura (1989); Weisman (1992)]. Rotunno et al. (1988) and Weisman et al. (1988) demonstrate that the time period over which this evolution takes place depends on both the strength of the convectively generated cold pool and the strength of the low-level ambient vertical wind shear, with large, upshear-tilted systems most readily produced for environments of large CAPE and weak-to-moderate ambient vertical wind shears. The inclusion of the Coriolis force in such quasi-two-dimensional simulations does not fundamentally alter this evolution, but additionally allows for the development of a two-dimensional cyclonic shear zone at midlevels within the stratiform precipitation region and an anticyclonic shear zone aloft, and also acts to limit the horizontal scale of the system (e.g., Fovell 1991).

The simulations presented herein represent a next step in the nonhydrostatic convection-resolving modeling studies and attempt to bridge the gap between the idealized quasi-2D studies and the 3D mesoscale modeling studies. Our underlying philosophy is to add only what is necessary to the idealized models in order to reproduce the 3D asymmetric convective systems. Following this approach, we retain the idealized horizontally homogeneous environments while removing the restriction of along-line periodicity. The initial convective lines are finite in length and are free to evolve and choose their scale. As shall be shown, the resulting systems bear strong resemblance to observed symmetric and asymmetric MCSs and MCCs.

The first question we address is whether finite-length squall lines evolve differently than their infinite length counterparts and whether these differences are consistent with observations. These basic questions are considered in section 2, where we discuss the evolution of a simulated squall line 200 km long in an environment with no Coriolis forcing and weak vertical wind shear. This simulation reproduces the general evolution depicted in the previous studies, but produces a stronger cold pool in the central portion of the system and also develops significant cyclonic and anticyclonic circulation at midlevels behind the northern and southern ends of the line, respectively. The bias in the cold pool strength, along with the midlevel circulation that concentrates and strengthens the rear inflow current at the core of the system, leads to a bow-shaped system with the strongest convection located at the apex of the bow. In section 3 we present results from a similar simulation that includes the Coriolis forcing. This simulation reproduces many of the features associated with long-lived MCSs and MCCs, including anticyclonic outflow aloft and a midlevel MCV located behind the northern end of the system. A more detailed analysis of this squall line evolution is presented in sections 4 and 5, including an analysis of MCV formation and the interaction between the convective and system-scale circulations. Further discussion and a summary follow in section 6.

2. MCS simulation without earth's rotation

a. Model description and experimental design

The 3D squall line simulations were performed using the interactive adaptive-grid cloud model described in Skamarock and Klemp (1993). The model resolves both the convection and the larger-scale squall line circulation by using multiple, overlapping, nested fine grids. Features not resolved on the coarser grids are resolved within the finer grids, with the number of fine grids, their size, and location being periodically updated during the simulation. Grids on the same refinement level may overlap, and multiple grids can be used to resolve long, curved features such as outflow boundaries. The model equations and discretization are identical to that described in Miller and Durran (1991). The Klemp and Wilhelmson (1978) time-splitting technique is used to solve the fully compressible system.

The effects of moisture are modeled explicitly using vapor, cloud, and rainwater. The model contains no ice. In this study, the model domain is a Cartesian f plane with a flat lower boundary. The lower and upper boundaries are free-slip and no boundary layer parameterization is used.

The coarse-grid domain has a horizontal extent of 1080 km × 1080 km and a vertical extent of 17.5 km for all simulations. The coarse grid has a horizontal grid spacing of 18 km and a vertical grid spacing of 700 m. Open lateral boundary conditions are used on the coarse grid (Klemp and Wilhelmson 1978). Two levels of refinement are included within this domain: the first level has a horizontal grid spacing of 6 km and the second level a horizontal grid spacing of 2 km. The vertical resolution remains the same on all grid-refinement levels. In general, the different level grids interact in the traditional two-way interactive nested-grid approach. Grid placement is accomplished by examining the evolving flow periodically and replacing, adding, or removing grids such that the active convection is always contained within grids having 2-km horizontal resolution. The solution was examined every 20 minutes for purposes of grid replacement. In most cases the finer-grid axes are aligned with the coarse grid, but this need not be the case. Examples of grid placement are shown in the presentation of the simulations.

The environment for these simulations is initially horizontally homogeneous, with the thermodynamic sounding shown in Fig. 3 (taken from Weisman and Klemp 1982). We begin with an examination of weak shear cases because observational evidence indicates that long-lived MCSs often form in weak shear environments with generally weak large-scale forcing. The initial winds are east–west only, increasing linearly from zero at the surface to 10 m s^{-1} at 2.5 km, and remaining constant at 10 m s^{-1} above 2.5 km. Convection is initiated using a north–south line of six warm thermals spaced at 40-km intervals. The thermals are centered at z = 1.4 km and the perturbation potential temperature decays from a 2 K excess to zero at 10 km horizontally and 1.4 km vertically from their centers. Small random perturbations are superimposed on the thermals such that the line departs from exact symmetry. While the convective initiation is nonphysical, after a few hours the line appears realistic and evidence of its initiation is no longer apparent.

b. *Overview of line evolution with $f = 0$*

In the absence of Coriolis effects, the only significant difference between this simulation and north–south periodic 3D simulations used in previous studies is the finite-line end effects. Simulated infinite-length 3D squall lines in a shallow, weak shear environment (cf. Weisman et al. 1988) evolve from an initially downshear tilted convective system into an upshear tilted system that ultimately weakens after the strengthening cold pool surges out ahead of the line, as illustrated in Fig. 2. Three-dimensional along-line periodic squall line simulations with the present interactive model also reproduce this evolution, as does the following more fully 3D simulation.

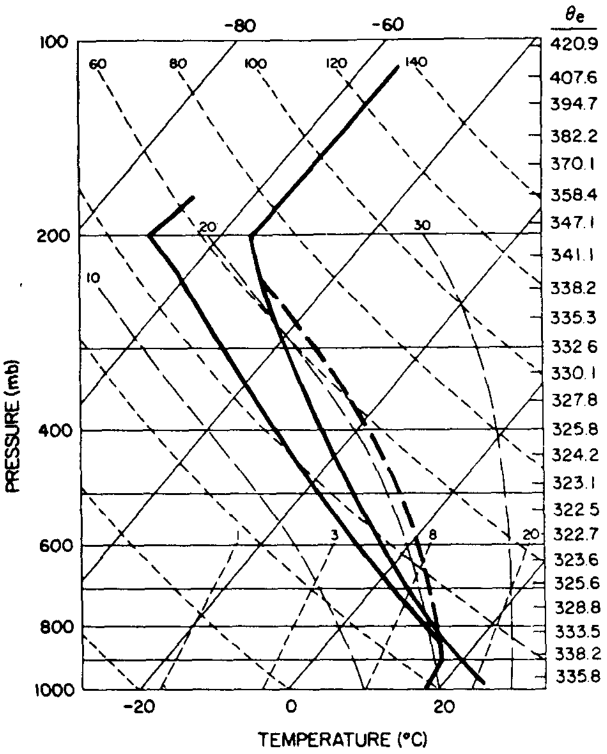

FIG. 3. The thermodynamic sounding used for all the simulations presented herein. Model levels are denoted by tick marks on the right and the corresponding values of θ_e are listed. The sounding has a CAPE of 2400 m^2 s^{-2} and a surface mixing ratio of 14 g kg^{-1}.

The general evolution of the finite length line is depicted in Fig. 4, which also illustrates the placement of the finest-resolution grids. The line evolves from one of approximately 200 km in length at 2 h to several hundred kilometers in length by 6 h, with the strongest convective activity located in the central 100 km of the line and weaker convection existing on the flanks. Only three fine grids are needed at 2 h to resolve the line, whereas five fine grids are needed at 6 h. The general symmetry of the system is maintained even though the line is not constrained to remain symmetric.

The flow fields at z = 350 m, 3000 m, and 8000 m at 2 h are shown in Fig. 5. The five cells evident in the figure have been initiated at the intersection of the gust fronts generated by the initial six cells. While the nonphysical nature of the convective trigger is still evident, some line-end effects are already noticeable. At the lowest level, the end cells have both stronger updrafts and downdrafts, along with stronger gust front winds, than the cells in the interior of the line. Over their life cycles and at all levels, the end cells at early times tend

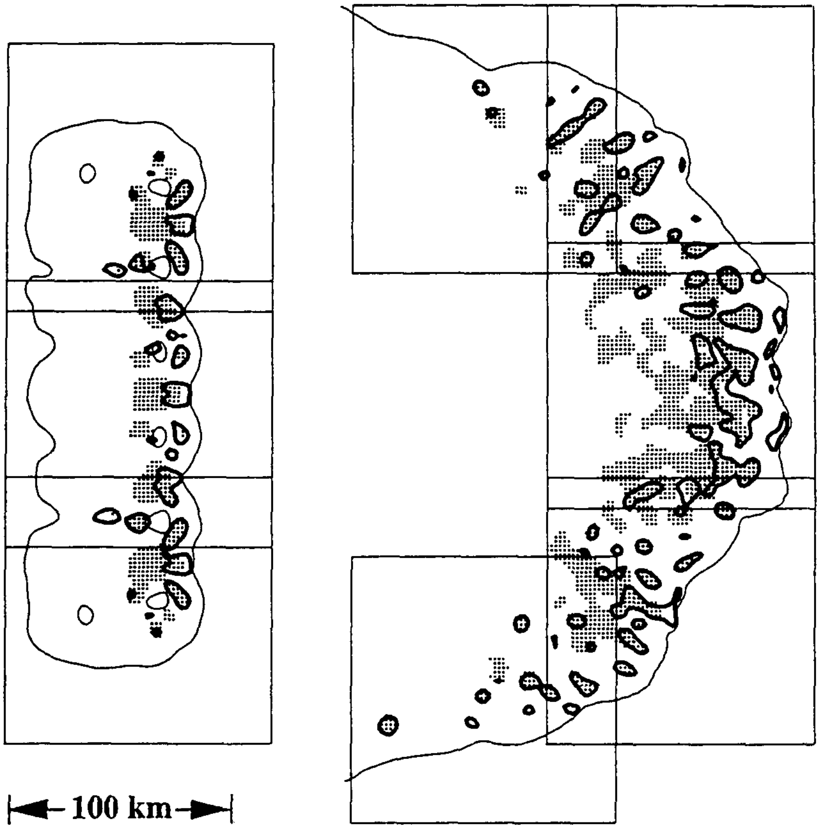

FIG. 4. Horizontal cross sections from the no-Coriolis simulations at 3150 m plotted in ground relative coordinates at 2 and 6 h. The surface gust front ($\theta' = -1$ K at $z = 350$ m) is the thin contour, $w = 2$ m s^{-1} is the thick contour, and the rainwater field $q_r > 0.5$ g kg^{-1} is stippled. The finest-resolution grids are included at both times.

to be stronger than the interior cells. We attribute this to the fact that the circulation associated with the interior cells is constrained to be quasi-two-dimensional while that associated with the outer cells is largely three-dimensional. Bjerknes (1935) was the first to suggest that 3D cells will be stronger than their 2D counterparts, a result that modeling studies have confirmed.

Figure 6 shows the system at 4 h. The cells are no longer strictly oriented along a north–south axis; rather, portions of the line north and south of the line center have surged out farther to the east. The line surges are a consequence of the relatively stronger cells at the line ends. The stronger cells produce stronger cold pools that lead to the enhanced outflow. This surging of the line ends is a ubiquitous feature in all the 3D finite-length squall line simulations in cases that are initialized with sufficiently long lines in this environment. Moreover, once the lines are sufficiently long (greater than 100 km in this environment), line length does not alter the line surge characteristics; however, the timing of the surges is significantly altered by the initial cell spacing, with line surging being delayed by a larger spacing between initial cells.

By 4 h, cyclonic and anticyclonic flows are apparent to the rear of the line at midlevels on the northern and southern line ends, respectively (Fig. 6b). The vorticity at midlevels is coincident with a turning, toward the east, of the inflow entering from the south on the southern line end (and vice versa for the inflow on the northern line end). Figure 6c reveals corresponding circulations of the opposite sign at upper levels in the outflow. As shall be shown later, these circulations are associated with line end effects and, when combined with Coriolis forcing, produce recognizable features of mature MCSs and MCCs.

Over time, the line surges progress from the line ends to the center. Figure 7 shows the low- and midlevel flow fields at 6 h. The two separate line surges have merged at the center of the line resulting in an approximately 100-km length line of strong convection and weaker flanking lines of convection trailing off to the SW and NW. The strongest surface gust front velocities (Fig. 7a) are associated with the central portion of the line. The midlevel rear inflow, shown in Fig. 7b, is now entering directly from the west and is focused into the center of the line. This stronger rear inflow is a direct result of the additive effects of the end circulations,

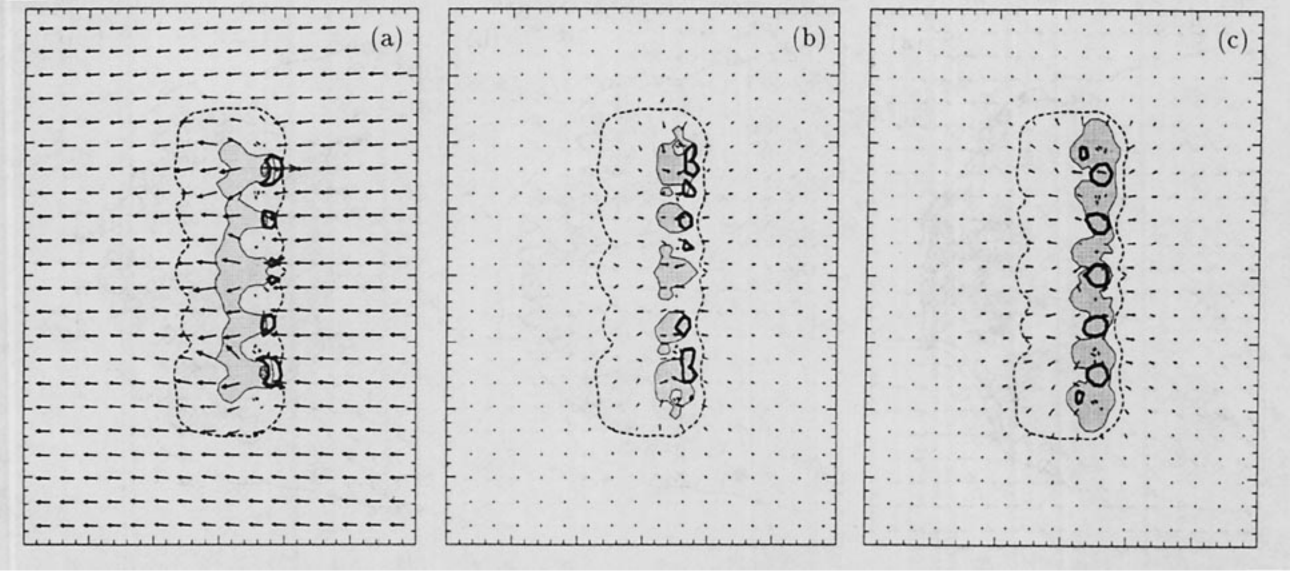

FIG. 5. Horizontal cross sections at (a) 350 m, (b) 3000 m, and (c) 8000 m for the no-Coriolis simulation at 2 h. The flow vectors are storm relative with a system velocity $\bar{U} = 10$ m s^{-1} and where a vector length of one grid interval is 8 m s^{-1}. The plotting domain is 300 by 400 km. The dashed line represents the -1 K θ' contour and denotes the cold pool–gust front boundary, plotted at all levels for reference. At 350 m (a), the thick contour is $w > 0.5$ m s^{-1}, $\theta' < -4$ K is highlighted by light stippling, and $\theta' < -6$ K is highlighted by dark stippling. At 3000 m (b), $w > 2$ m s^{-1} is contoured and rainwater greater than 0.5 g kg^{-1} is stippled. At 8000 m (c), $w > 2$ m s^{-1} is contoured and cloud water greater than 0.1 g kg^{-1} is stippled. The data are plotted on a 6-km horizontal resolution grid.

which serve to focus both the rear inflow and convection into the center. The cyclonic and anticyclonic flow at midlevels associated with the line ends has also strengthened over the 2-h period, as has the cyclonic and anticyclonic flow in the outflow region aloft (Fig. 7c). By this time the system has reached maturity and it evolves further only in that the flanking lines extend out farther to the SW and NW over time; the central region of strong convection maintains its strength and size.

Thus, we observe that the ultimate effect of the line ends is to focus the rear inflow into the central portion of the line, with the strongest rear inflow, cells, and line surge ultimately located in this region. The presence of line ends also leads to the development of mesoscale cyclonic and anticyclonic circulations at middle and upper levels. The midlevel circulations accentuate the focusing of the rear inflow and resemble the vortices that are simulated in stronger shear environments by Weisman (1993). The vortices described by Weisman

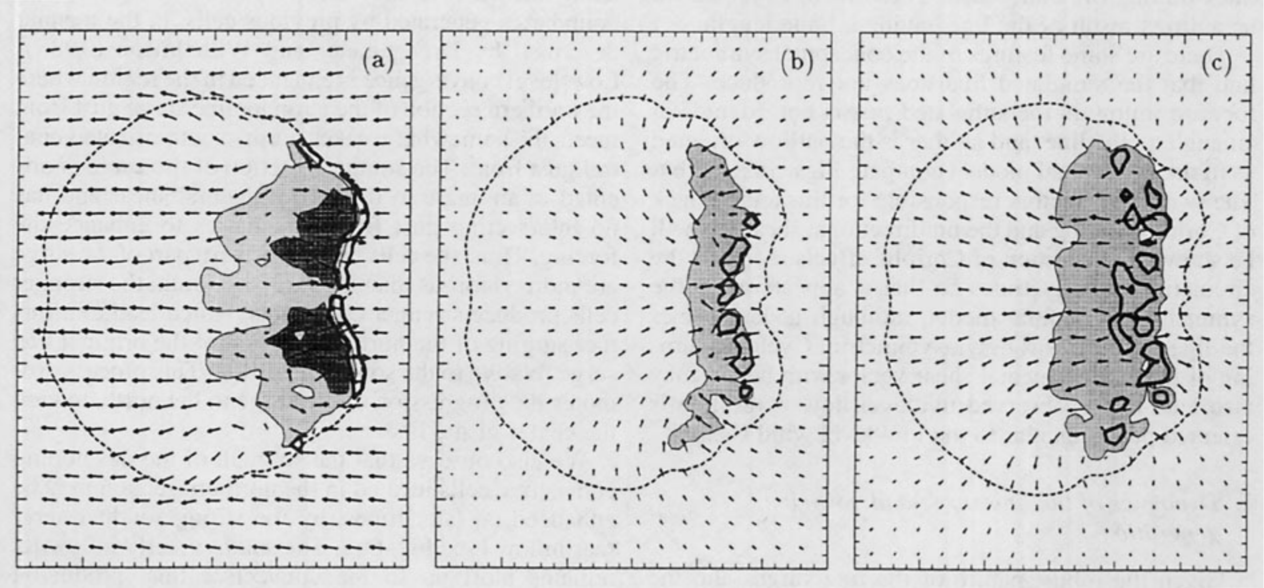

FIG. 6. As in Fig. 5 except at 4 h.

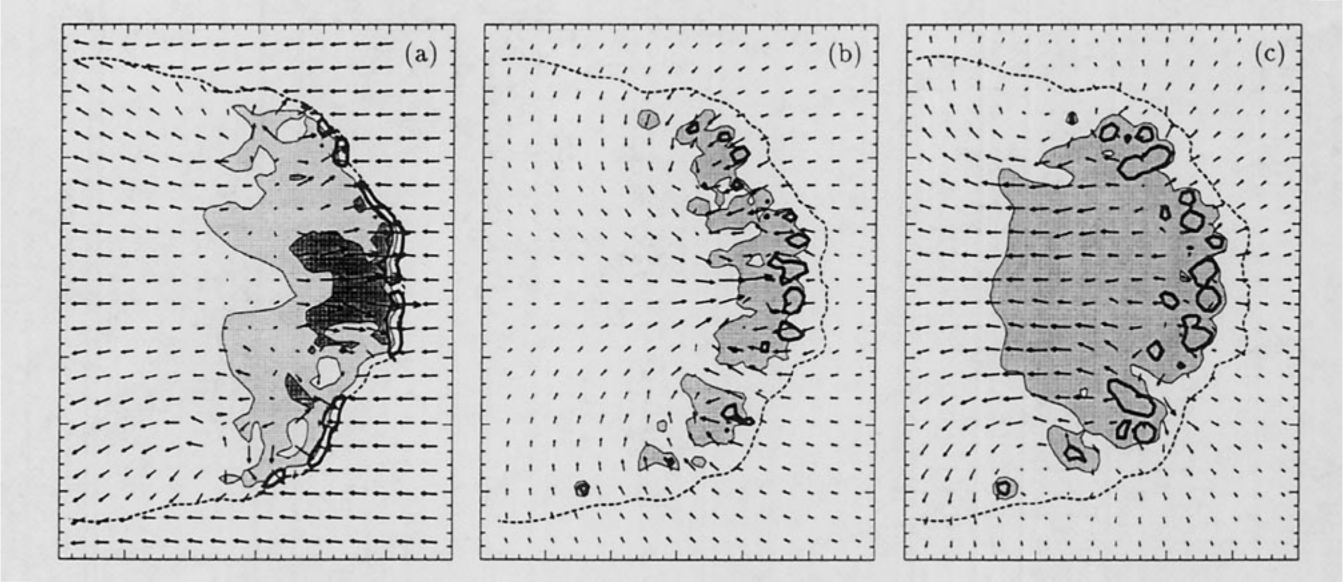

FIG. 7. As in Fig. 5 except at 6 h.

(called bookend vortices), however, are stronger and smaller in scale than the midlevel circulations described here, though both are associated with a bowing out of the convective system and strong rear inflow. Compared with the 3D periodic line, the convective cells in the central portion of the finite line are stronger and more erect.

The simulated line possesses many characteristics consistent with observed convective systems as depicted in the conceptual model of a symmetric line. As in the conceptual model in Fig. 1a, the mature system (Fig. 7) has convective elements at the line center that are stronger than the elements at the line ends. Also, the line itself bows out at the center with weak flanking lines trailing off both sides. These features appear to be a direct result of the line having a finite length.

There are some features of the conceptual symmetric line that the simulated line does not reproduce. The forward inflow in the simulated line is not oriented at an angle to the line, and neither is the outflow oriented as in the conceptual model (compare Figs. 1a and 7b). The two major factors responsible for this are the lack of Coriolis forcing and the unidirectional shear. As will be shown, the addition of Coriolis effects reorients the circulation at early times so that it appears as in the symmetric conceptual model, although at later times the line becomes strongly asymmetric. Cyclonic turning of the environmental shear vector with height may also lead to the observed midlevel flow if the line is oriented perpendicular to the low-level wind shear.

c. *Dynamics of the line surge and vorticity generation*

Given the robust nature of the line surges and the rear-inflow focusing, we examine these features in greater detail. In what follows, we consider the southern line surge, with the understanding that the northern surge behaves as the mirror image.

Initially, line-end cells are more vigorous than the interior cells due to their more three-dimensional rather than two-dimensional nature; low-level convergence and updraft velocities are greater than those of the interior cells. These stronger cells produce stronger cold pools, which lead to a surging of the line end. The initial surge is already evident at 2 h (Fig. 5a).

The progression of the line surge evolves as the convective cells along the northern portion of the surge become stronger relative to those on the southern portion of the surge. New cells are preferentially generated along the line at the intersection of the gust front boundaries generated by previous cells, in the manner described by Droegemeier and Wilhelmson (1985). Low-level convergence is enhanced in the region where the northern section of the stronger line surge gust front meets the somewhat weaker north–south oriented central gust front. The southern section of the surge is oriented at an angle to the environmental shear and has no intersecting gust front boundaries to enhance the forcing. Thus, the cells on the northern part of the surge are more vigorous than those on the south; the stronger cells produce stronger cold pools, which lead to a further surging of the northern portion of the original line surge relative to the southern portion. This process promotes the progression of the surge to the north, toward the center of the line.

We also observe that the strength of the developing convective cells located in the northern section may be enhanced, at later times, by the strong southwesterly rear inflow (see Fig. 6b). The southwesterly inflow jet remains aloft up to the convective line, producing deeper lifting at that location and leading to more erect, stronger convection (Weisman 1992). The jet, while focusing the rear inflow into the northern section of the convection associated with the line surge, also inhibits rear inflow into the southern portion of the line surge. Finally, the rear-inflow jet also descends to the surface, where it augments the gust front winds in the region where low-level enhanced convergence is observed. In this case the rear-inflow dynamics appears to be of secondary importance in driving the line evolution because the jet forms as a result of, and after, the convective enhancement in the northern section of the line surge, and is an effect rather than a cause of the convective bias.

In experiments with differing initial line lengths, we find that the simulated lines follow a similar evolution regardless of the initial line length. Longer initial lines take longer for the line-end surges to meet in the center and produce the final line configuration, while shorter initial lines (even starting with a single thermal) rapidly move toward this final configuration. Also, after a sufficient period of time, the lines of differing initial length evolve into systems of roughly the same size. We will examine this issue of scale selection in a future study.

There is vertical vorticity associated with the line-end cyclonic and anticyclonic circulations at middle and upper levels. Figure 8 shows the vertical vorticity at midlevels at 6 h. The rear portion of the line is dominated by positive vertical vorticity to the north and negative vertical vorticity to the south of the line center. The vertical vorticity is strong immediately behind the central region of convection with weaker vorticity found rearward of this region and rearward of the flanking lines.

With no ambient vertical vorticity present in the environment, horizontal vorticity must be tilted to produce this vertical vorticity. Vertical vorticity generation by the tilting of horizontal vorticity at $z = 3$ km and 6 h is given in Fig. 9a. Production by tilting is dominated by the presence of convection and gravity waves, and there is no clear signal showing preferential production of positive (negative) vorticity north (south) of the line center. The analysis of Davis and Weisman (1993) shows that, given the finite length of the squall line, there must be significant tilting associated with the descending rear-to-front and ascending front-to-rear flows. Their analysis does not reveal how that tilting takes place. In strong-shear environments, where "bookend" vortices are observed, a similar difficulty arises when trying to identify their source of vorticity at later times when the vortices are not associated with convective updrafts or downdrafts (Weisman 1993). Moreover, the stretching of vertical vorticity, depicted in Fig. 9b at $z = 3$ km and 6 h, exhibits the expected antisymmetry behind the leading-line convection, in the region where the front-to-rear and rear-to-front flows are ascending and descending through this level.

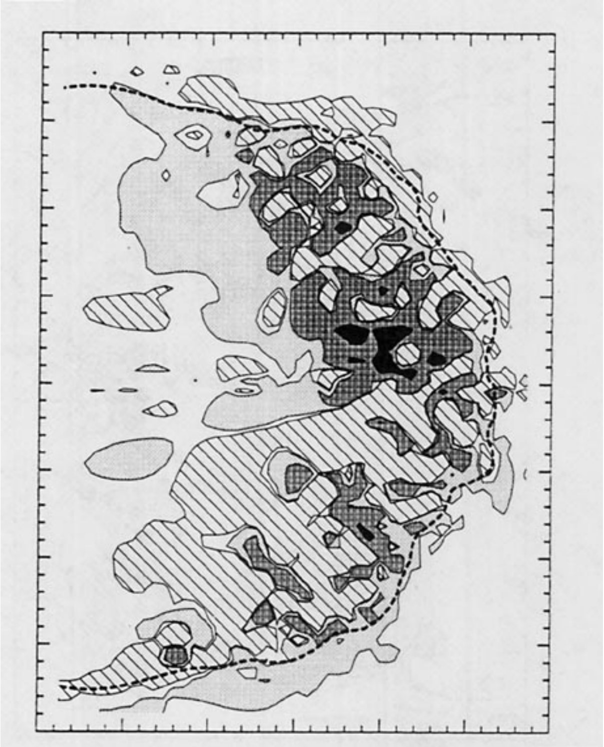

FIG. 8. Horizontal cross section of vertical vorticity at 3000 m and 6 h for the no-Coriolis simulation. Stippling, from light to dark, denotes vorticity greater than 0.1×10^{-4} s^{-1}, 1.0×10^{-4} s^{-1}, and 10.0×10^{-4} s^{-1}. Parallel lines indicate vorticity less than -0.1×10^{-4} s^{-1}.

Apart from convective tilting of horizontal vorticity, we have identified two other sources of vertical vorticity produced by tilting. First, at lower levels there is tilting of the base-state horizontal vorticity in the rear inflow, because the rear inflow also enters from the north and south as well as from the west. Figure 10a depicts the horizontal vorticity vectors, equivalent potential temperature θ_e, and streamlines for the rear inflow at $z = 2$ km at 6 h. In the rear inflow θ_e is conserved, and the environmental θ_e is decreasing up through 6 km (see Fig. 2). Thus, areas of descent in the rear inflow are indicated by decreasing θ_e in the horizontal plane. The tilting of streamwise vorticity into the vertical results in vertical vorticity of the proper sign in the regions that are shaded in the figure. While the magnitude of the vorticity generation is small and occurs only at intermediate and later times, it occurs over a large region. Second, there is also tilting of the horizontal vorticity generated by horizontal buoyancy gradients associated with the outflow and rear inflow. Figure 10b, showing the same fields at $z = 3.5$ km, reveals significant tilting of streamwise vorticity from rear inflow entering from the west-southwest and west-northwest. Again, the magnitude of the vorticity generation is small, but it occurs over a large region. The rear inflow trajectories passing through both these

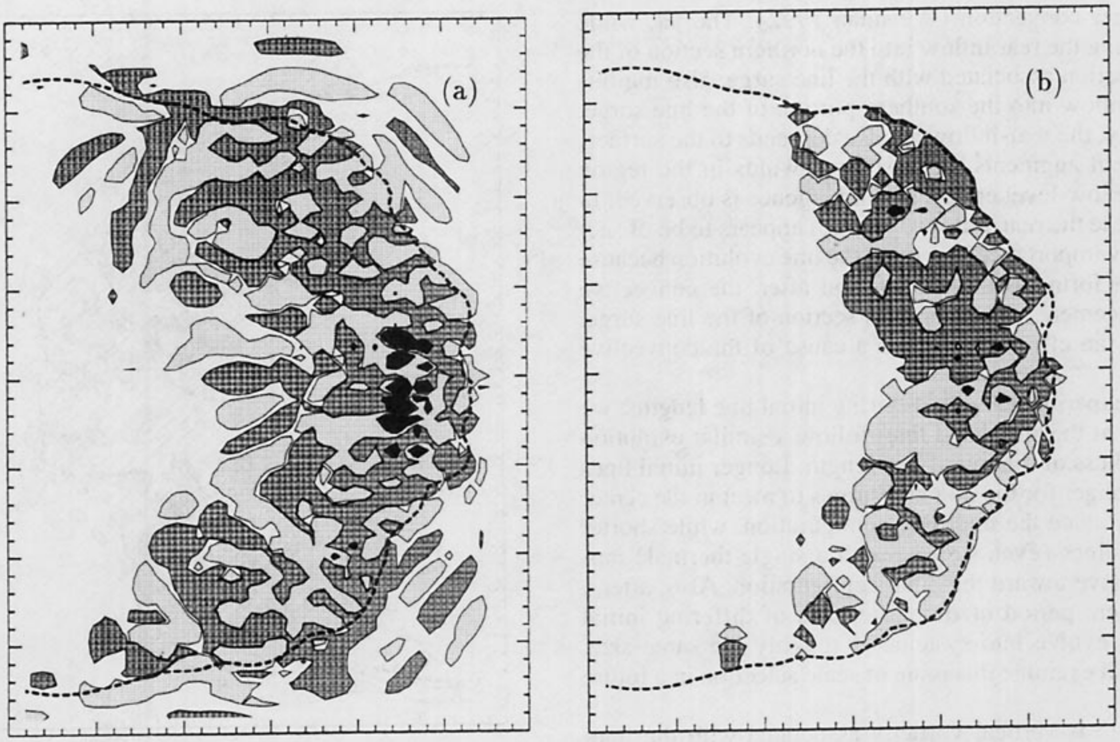

FIG. 9. Vorticity generation at 6 h and z = 3000 m by (a) tilting of horizontal vorticity and (b) stretching of vertical vorticity. Light stippling denotes values less than -1×10^{-8} s^{-2}, dark stippling denotes values greater than 1×10^{-8} s^{-2}, and the filled regions denote tilting or stretching with absolute values greater than 1×10^{-6} s^{-2}.

regions often continue into the region of stronger vorticity directly behind the central region of convection; hence, subsequent advection and stretching of this vorticity may account, in part, for the much larger vorticity observed in the central region.

3. MCS simulation including earth's rotation

a. Initial state

The following simulation is identical to that described in section 2 except that the Coriolis parameter $f = 10^{-4}$ s^{-1}. In the previous simulation, the horizontally homogeneous base state, with $f = 0$, satisfies the equations of motion and is considered balanced; the flow, if unperturbed, remains unchanged. To the degree that the initial state is steady, two balances need to be considered in the weak, shallow shear case when f is nonzero: thermal wind balance, which is a combination of the geostrophic balance and the hydrostatic balance, and a balance among the shear stresses in the planetary boundary layer, the horizontal pressure gradient, and the Coriolis force, which in its simplest form results in the Ekman turning of the winds.

If the base-state east–west wind shear is in thermal wind balance, there would be a south-to-north temperature gradient of approximately -1.1 K/100 km over the depth of the shear layer. This horizontal temperature gradient results in decreasing CAPE to the north along with increasing vertical temperature gradients at the top of the linear shear layer, which represents an increasingly strong convective cap between the shear layer and the uniform flow aloft. Conversely, there would be increasing CAPE to the south along with decreasing (or negative) stability at the top of the shear layer. If the sounding in Fig. 3 is centered in the domain, then physically unrealistic soundings occur in the north and the south, and significant differences in convective potential occur along the initial line. There would also be horizontal advection of this north–south temperature gradient by the convectively generated velocity field, but this is a small effect compared with the convective bias.

The second balance is that among the shear stresses in the planetary boundary layer, the horizontal pressure gradient, and the Coriolis force. If these forces constitute the entire balance and if the eddy viscosity is assumed constant, then an Ekman spiral occurs across the boundary layer where the magnitude of the v velocity component (the component perpendicular to U_g, the geostrophically balanced uniform flow above the shear layer) reaches a magnitude that is approximately 30% of U_g. Boundary-layer observations show that the magnitude of v is often closer to 15% of U_g (Brown 1970).

Observations reveal that pre-MCS environments are often largely in thermal wind balance, particularly in

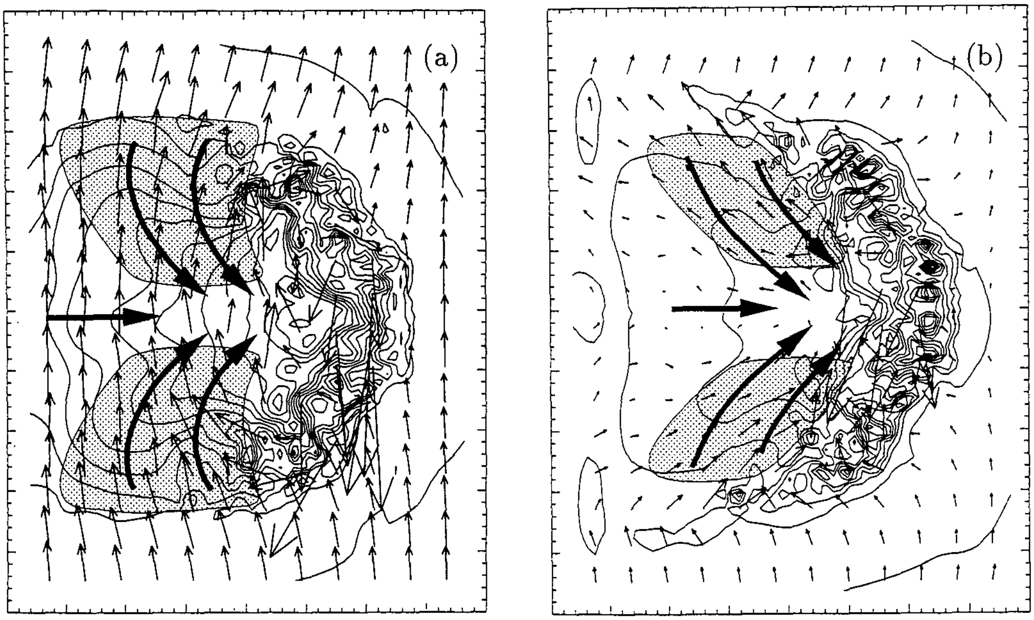

FIG. 10. Horizontal cross section depicting vertical vorticity generation through tilting of horizontal streamwise vorticity at (a) 2000 m and (b) 3500 m at 6 h. Horizontal vorticity vectors are plotted where a vector length of one grid interval denotes a vorticity of 8×10^{-4} s^{-1}, and θ_e is contoured in increments of 1 K. Decreasing θ_e in the plane indicates descent and tilting of the streamwise horizontal vorticity in the stippled regions along the average streamlines depicted as bold lines. The domain plotted is 400 km by 500 km.

deep shear cases, and also in some weak shear cases [e.g., the 8 June 1980 HIPLEX MCC in Leary and Rappaport (1987), their Fig. 3]. However, other observations suggest that pre-MCS environments that exhibit weak shears often lack any obvious thermal wind balance [e.g., the 23–24 June 1985 PRE-STORM MCS in Johnson and Bartels (1992), their Fig. 3]. Both thermal wind balance and an Ekman balance are likely to be present in pre-MCS environments in varying degrees, along with small- and large-scale unbalanced transient motions.

We wish to increase the simulation complexity as little as possible while still including the fundamental influences of the Coriolis force. Thus, we have chosen not to impose a thermal wind balance on our initial state so as to avoid the physically unrealistic soundings, maintain the uniform shear, and not introduce any convective bias along the line. Instead, we assume that our base state is primarily in approximate Ekman balance, with the approximations that v is ignored and that there is a linear approximation to the Ekman layer u in the shear layer (we do recognize that a boundary layer 2.5 km deep is significantly deeper than what is commonly observed). We have chosen this state in order to permit the investigation of a developing convective system in an environment containing a horizontally homogeneous convective potential along with unidirectional wind shear that can be compared meaningfully with corresponding simulations without Coriolis effects. Although we recognize that these atmospheric conditions represent a gross simplification of observed convective environments, we believe that the simplifications are justified in seeking to evaluate some of the fundamental mechanisms by which Coriolis effects organize the evolution and structure of MCSs. Given the assumed balance for the mean-state variables, the model will correctly simulate the evolution of perturbations from that mean state; an exact mean-state balance, in terms of the model numerics, is not needed for the simulations.

b. Overview of line evolution with Coriolis effects

The general evolution of the Coriolis-influenced system is shown in Fig. 11, which depicts the convective evolution at 2, 6, and 10 h in ground-relative coordinates. The system exhibits significant asymmetries compared with the system in the no-Coriolis simulation (Fig. 4). In particular, there is strong growth of the southern flank of the Coriolis-influenced system along with a decay of the convection along the northern flank. This leads to a system reorientation and system motion to the right of the ambient shear vector.

Figure 11 also depicts the fine-grid positions at the three times. At 10 h, 9 fine grids are used to resolve the convective line, with three being rotated with respect to the base grid. A total of 13 grids are used at 10 h; one coarse grid (dx = 18 km), three middle-level grids (dx = 6 km), and nine finest-level grids (dx = 2 km).

At early times the Coriolis and no-Coriolis runs are almost identical, but by 4 h the differences are notice-

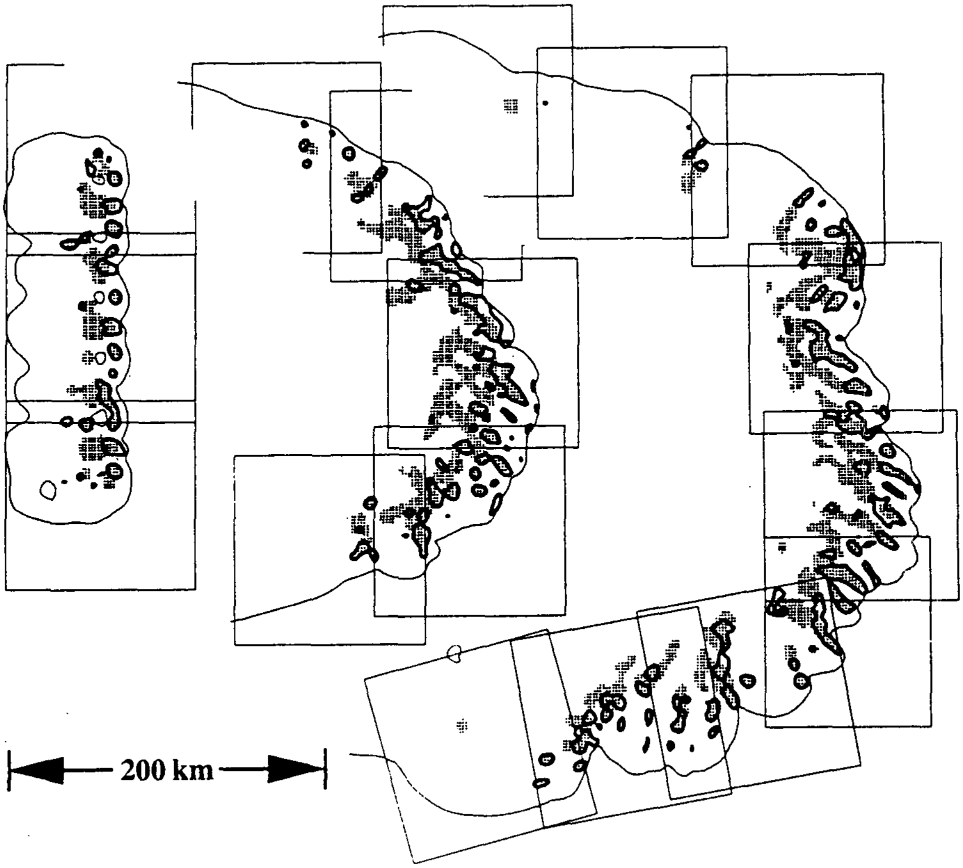

FIG. 11. Horizontal cross sections from the Coriolis simulations at 3000 m plotted in ground-relative coordinates at 2, 6, and 10 h. Plotted as in Fig. 4. Note the strong system growth and migration toward the southeast. The finest-resolution grids are included at the three times.

able. Figure 12 shows the horizontal flow fields at 350 m, 3000 m, and 8000 m at this time, and can be compared with the no-Coriolis case depicted in Fig. 6. Generally, these differences arise because the perturbation winds in the Coriolis case are turning to the right relative to the winds in the no-Coriolis case, with this effect being most pronounced at the middle and upper levels. This turning causes the cyclonic (anticyclonic) circulation at midlevels on the northern (southern) end of the line to be amplified (repressed). In particular, the rear inflow associated with the northern line surge has a NW–SE orientation while the rear inflow associated with the southern line surge is oriented E–W. Also note that the flow is from the southeast out ahead of the line at midlevels in the Coriolis simulation, as opposed to being directly from the east as is the case in the no-Coriolis simulation. A similar Coriolis effect occurs at the 8-km level except that the anticyclonic circulation is enhanced. At the surface, the gust front winds are also beginning to turn to the right relative to those in the case without Coriolis effects.

Another significant difference between the simulations is evident in the line surges on the northern and southern line ends. While the surges are of equal strength in the no-Coriolis simulation, the southern line surge pushes out more strongly than the northern line surge in the simulation with Coriolis forcing.

The flow fields at 6 h are given in Fig. 13. The line now has a northern flank oriented NW–SE and a southern flank oriented along a SW–NE axis. The flanks of the line have grown considerably, and the system has migrated south in response to the strong southward flow in the cold pool behind the surface gust front. At this time, the midlevel MCV first becomes clearly apparent. The MCV is evident in the strong cyclonic circulation located on the northern flank of the line, centered on a region of active convection. Associated with the MCV is strong rear inflow over a 100–120 km section of the line. The southern rear-inflow jet, visible at 4 h in Fig. 12b and associated with the southern line surge, has progressed to the northern end of the line and is now situated in the southeast quadrant of the MCV. The upper-level outflow is predominantly to the north-northeast (Fig. 12c) with strong anticyclonic circulation evident in all regions except for the remnant of cyclonic circulation rearward of the southern flank.

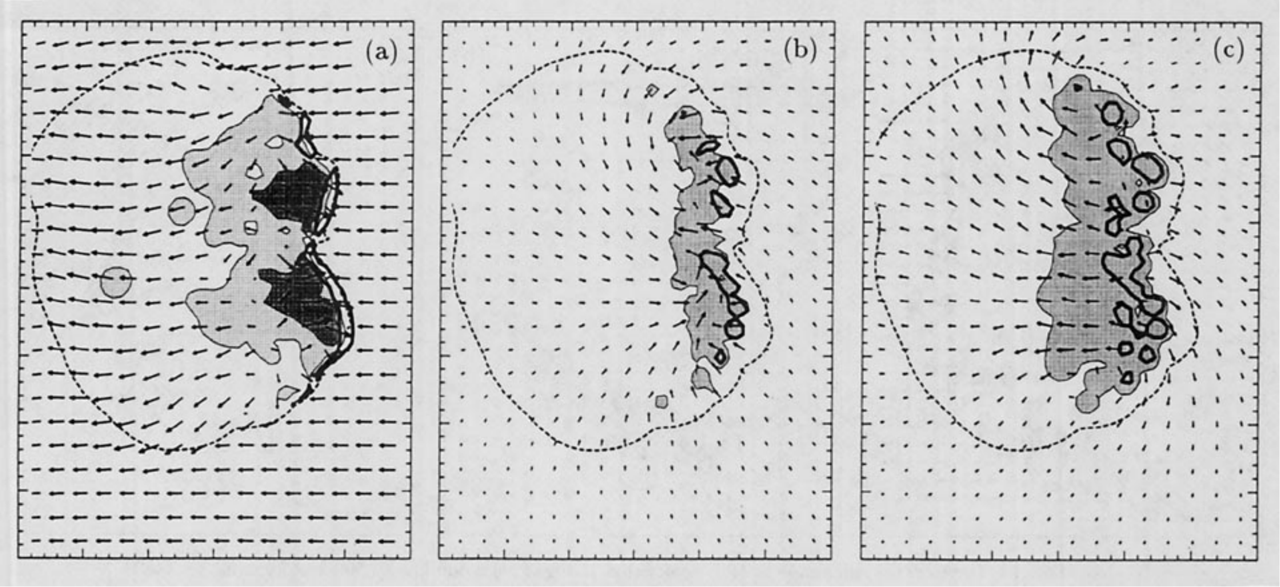

FIG. 12. The Coriolis simulation at 4 h, depicted as in Fig. 5.

The formation of the MCV and the coherent, mesoscale rear inflow, along with the migration of the southern rear-inflow jet to the southeast quadrant of the MCV, leads to several major events in the MCS evolution that are apparent in comparing the midlevel flow fields at 6 and 10 h (Figs. 13b and 14b). First, the line east and southeast of the midlevel MCV has surged strongly to the east. This occurs simultaneously with the decay of the convection directly north-northeast of the MCV. This evolution produces a squall line with two distinct segments: one oriented N–S and another SW–NE. Second, the line surge has left behind the MCV that had previously been centered in the region of active convection. The MCV is associated with a strong rear-inflow jet located almost directly east of the MCV. The northern terminus of this rear-inflow jet is coincident with the strongest convection in the system, located on the northernmost section of the active, leading-line convection. Finally, the MCS has also grown dramatically over this 4-h period, particularly along its southern flank. The leading-line length has approximately doubled from 200 km at 6 h to one extending over 400 km at 10 h. Figures 14a and 14c show the surface and upper-level flow fields at 10 h. At the surface is a mesohigh with the characteristic divergent flow. The strongest gust front velocities are now lo-

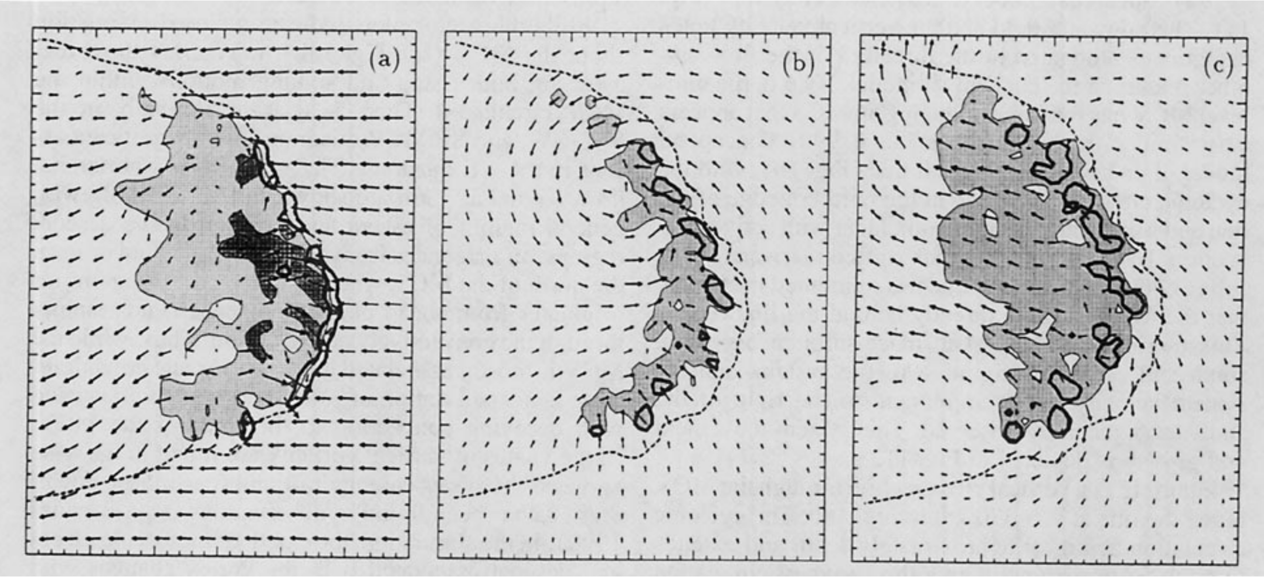

FIG. 13. The Coriolis simulation at 6 h, depicted as in Fig. 5.

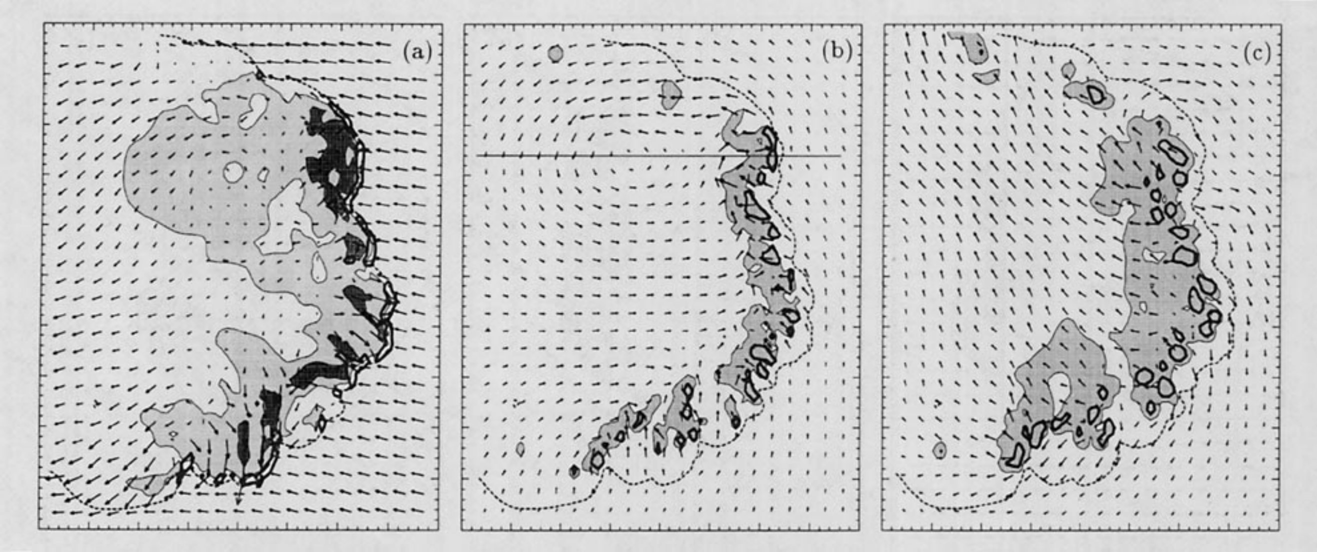

FIG. 14. The Coriolis simulation at 10 h depicted as in Fig. 5 on a 400 km by 500 km domain.

cated in the southeastern section of the line where the line is growing most rapidly. This growth has led to a southward migration of the system. Strong anticyclonic circulation aloft continues to develop, with the strongest outflow from the rear of the system, heading NW directly above the MCV.

c. Comparison with observations

At early times the system takes on the appearance not of an asymmetric MCS but of the symmetric system illustrated in Fig. 1a; even at 4 h the line appears somewhat symmetric. It differs from the no-Coriolis simulation, however, in that the flow field at midlevels has the WNW–ESE orientation, as in the Houze et al. (1990) conceptual model of a symmetric system (Fig. 1a). The rainwater field and the vertical velocity fields depict cells elongated in the direction of the flow, another feature in the conceptual model. By 6 h, the midlevel MCV has formed, producing an MCS that appears very similar to the Houze et al. (1990) conceptual model of an asymmetric squall line (Fig. 1b), with the cyclonic circulation located at the northern edge of the line and a circulation center coincident with active convection. By 10 h the MCV has shifted rearward of the active convection and the line has reoriented itself such that the MCV is more directly behind the line center. This reorientation has taken place through a general south and eastward migration of the system, and the system velocity has a component to the right of the shear as is generally observed. This system movement and growth is depicted in Fig. 11.

Figure 15 is a vertical cross section through the MCV along the line at $y = 370$ km in Fig. 14b. The cyclonic circulation begins at approximately 1 km and extends through 6 km vertically, with the strongest circulation located at the 2.5-km level. The region of positive vorticity is a few hundred kilometers in diameter, though the cyclonic circulation extends a few hundred kilometers beyond this. Thus, the horizontal and vertical extent of the MCV is similar to those observed.

The midlevel mesolow in the center of the MCV (Fig. 15b) is primarily the hydrostatic response to the positive buoyancy anomaly aloft and the negative buoyancy anomaly below the middle level of the vortex. The coincidence of the vortex with a region of enhanced stability is dynamically more significant. This stability, combined with the positive vorticity, indicates the presence of a positive potential vorticity (PV) anomaly coincident with the MCV. Calculations show that the PV anomaly accounts for a substantial portion of the MCV circulation, and as such the vortex represents a balanced flow (Davis and Weisman 1993).

While the vector plots indicate a closed circulation about the MCV (see Fig. 14b) trajectories show that there are both rising and sinking motions within the MCV circulation. There is descent generally in the NW, SW, and SE MCV quadrants, with significant ascent in the NE quadrant. The vorticity and horizontal flow vectors at 3 km are shown in Fig. 16 along with general regions of ascent and descent. In the descent regions, air originates from upper levels behind or from the north of the MCS, whereas in the ascent regions air originates from ahead of the line and ascends rapidly through the convectively active region. Thus, while the MCV is mostly associated with a mesoscale downdraft, there is a small region of ascending motion associated with decaying convection to the ENE of the MCV. Large values of vertical vorticity are found in the zone between the mesoscale updraft and rear-inflow downdraft, as has been found in observations (e.g., Brandes 1990). In the simulation, the extent of mesoscale ascent and descent associated with the vortex changes with height; at higher levels more of the vortex is associated

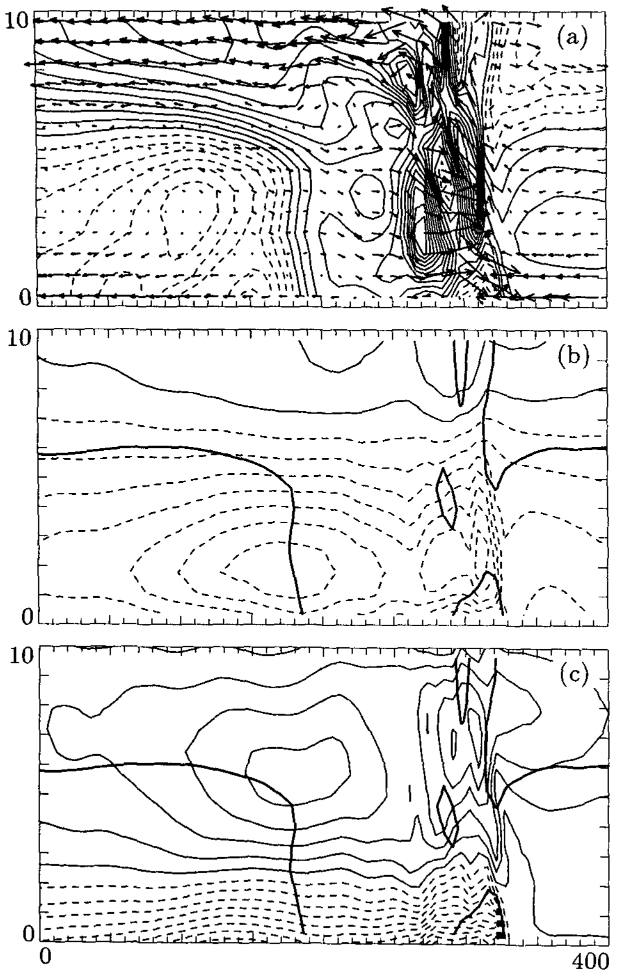

FIG. 15. West–east vertical cross sections through the MCV depicted in Fig. 14b at $y = 370$ km. In (a), the north–south velocity v is contoured with a 1 m s^{-1} interval; negative values denote flow out of the page. The pressure is contoured in (b) with a 0.5-mb interval. The bold contour is $v = 0$, and also depicted in (c) is the buoyancy, contoured with a 0.025 m^2 s^{-1} interval. The plotted domain extends 400 km in x and 10 km in z.

with ascending flow, and at lower levels more of the vortex is associated with descending flow.

In a case study of the 23–24 June 1985 OK-PRE-STORM MCS, Johnson and Bartels (1992) find that the northern end of the convectively active region was coincident with the central circulation of an MCV. Dual-doppler analyses with 2-km resolution showed that the maximum vorticity was located between a descending rear-to-front flow and an ascending front-to-rear flow with peak vorticity values of 60–80f. As in the Johnson and Bartels study, the vorticity maxima in Fig. 16 are found between the regions of mesoscale ascent and descent and the largest values are associated with active convection. Outside of convectively active regions, the peak vorticities are of the order of several f, that is, an order of magnitude smaller than those in the active convection. These smaller values are consistent with the smaller values reported in meso- and synoptic-scale observations (e.g., Brandes 1990; Menard and Fritsch 1989) and mesoscale modeling studies (e.g., Zhang and Fritsch 1987; Zhang 1992), where the resolution is on the order of a few tens of kilometers. Higher values are unlikely because these studies do not resolve the convection.

Small-scale vortices exhibiting closed circulation are found in the vicinity of the cyclonic circulation center throughout the line evolution up until the northeastern section of the line surges to the east (after 6 to 8 h). An illustration is given in Fig. 17, showing two small-scale vortices at midlevels at 5 h. The vortices are similar in scale to those observed by Verlinde and Cotton (1990) and Stirling and Wakimoto (1989). Other simulations of this type with differing shear profiles suggest that these convective-scale vortices are common, and they are also common in 3D periodic squall line simulations (Weisman et al. 1988). They are transient in nature, existing as a single entity for a few hours at most, and appear to have little impact on the overall evolution of the system.

4. Evolution of the leading line convection

In the simulation without Coriolis effects, the system-scale circulation leads to an enhancement of convection at the line center, with weaker convection along the trailing flanks. At early times, the simulated line that includes the Coriolis effect evolves similarly. In particular, the line surges progress toward the line center, and on the system scale the cyclonic and anticyclonic circulations at middle and upper levels are evident. At later times, however, the north–south line symmetry breaks down with the convection in the

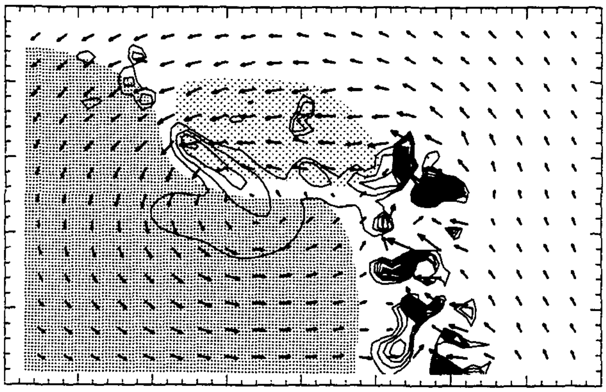

FIG. 16. Cross section of the vertical vorticity and horizontal flow field at 3000 m and 10 h for the northern end of the system from the Coriolis simulation. The lightly stippled area denotes a region of upward motion and the darkly stippled region denotes downward motion. Only positive vorticity is contoured and a $2f$ interval is used. Vorticity greater than $10f$ is filled. Flow vectors are depicted as in Fig. 5. The domain plotted is 400 km × 250 km.

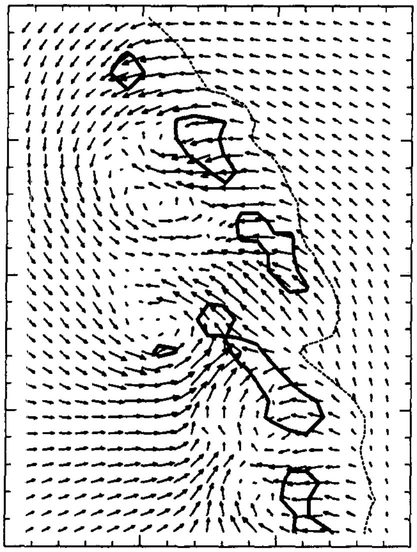

FIG. 17. Flow field on a horizontal cross section at 3000 m and 5 h from the Coriolis simulation. The plotted domain is 150 by 200 km and is centered over northern section of the line. A vector length of one grid interval corresponds to a speed of 17 m s^{-1}.

southern section growing in extent and eventually strengthening while convection in the northern section decays.

We believe that the evolution of the leading-line convection is primarily driven by the cold pool expansion, with Coriolis forcing playing an essential role in the southward propagation of the system. Relative to the no-Coriolis case, the low-level flow fields for the Coriolis simulations at 4 and 6 h show the increasing southward turning of the gust front winds (compare Figs. 6a, 7a, 12a, and 13a). The southern bias of the cold pool strength is also evident in the Coriolis simulation. The southward turning of the gust front winds combined with the colder and deeper cold pool found in the southern section of the system leads to enhanced convergence and deeper lifting in the southern section of the line, with the opposite effects occurring in the northern section of the line. This bias is self-reinforcing as enhanced convection on the southern line section strengthens the cold outflow, promoting further surging of the line to the south and continued convective enhancement. Conversely, reduced and shallower convergence in the north leads to weaker convection and a weaker cold pool, further weakening the convergence and frontal lifting.

To demonstrate how cold pools expand under the influence of Coriolis forcing, we present results from a simple numerical experiment. Figure 18 represents the low-level flow field and temperature at 8 h in a dry simulation using the nonhydrostatic model. The simulated domain is 320 × 320 km with dx, dy = 4 km and dz = 500 m, where the atmosphere is initially neutrally stable and horizontally homogeneous with $\theta_0 = 300$ K. A cooling function

$$S = -10\,\mathrm{h}^{-1}\left\{1 - \left[\left(\frac{x - x_c}{x_l}\right)^2 + \left(\frac{y - y_c}{y_l}\right)^2 + \left(\frac{z}{z_l}\right)^2\right]^{1/2}\right\} \qquad (1)$$

is activated at $t = 0$, where $x_l = 12$ km, $y_l = 40$ km, and $z_l = 2500$ m, and x_c and y_c are the coordinates of the cooling function center. Here S is set to zero when the right-hand side of (1) is greater than zero. A mean wind of $U = -10$ m s^{-1} is used to retard the propagation of the cold pool to the east; there is no shear in the environment. As can be seen in Fig. 18, most of the cold air is advected south of the centerline. The cold pool to the south is stronger and deeper than that in the north, and vertical velocities along the gust front in the south are also stronger (by ~30%) and produce deeper lifting than those in the north. The southern surge of the cold pool is not as great as that in moist simulations. We attribute the greater relative surge in the moist simulations to the positive feedback from convective downdrafts discussed previously.

The cold pool expansion described here depends on the existence of a mean wind relative to the cold air source, the mean wind acting to keep the cold air source close to the leading edge of the gust front. For example, in the absence of a mean wind, the cold pool expands

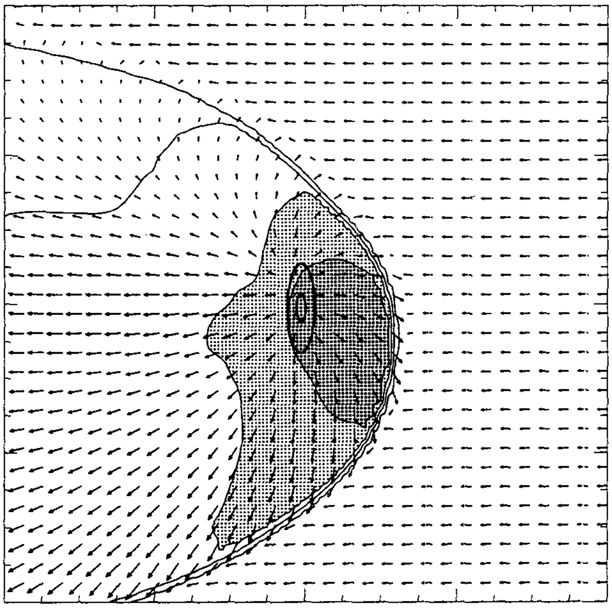

FIG. 18. Flow field and θ' at 250 m and 8 h for the dry simulation: θ' is contoured with an interval of 2 K and is lightly stippled for $\theta' < -4$ K and darkly stippled for $\theta' < -6$ K. The bold contours denote the cooling function at -4 and -8 K h^{-1}. The domain plotted is 320 km by 320 km, and vector magnitude of one grid length (20 km) is 35 m s^{-1}.

in all directions and develops a strong azimuthal velocity component. While an asymmetry exists because the cold air source is not circular, asymmetrically enhanced or repressed zones of convergence are very small in magnitude and no significant asymmetric propagation occurs. In the moist simulation the cold air source, that is, evaporatively cooled downdrafts, is always found close to the gust front; thus, the cold air sources move with the gust front.

As in the no-Coriolis simulation, we also observe that developing convective cells may be enhanced by the presence of strong rear inflow. In particular, there is a strong southwesterly inflow jet that progresses to the north of line center by 6 h and is coincident with enhanced convection, and by 10 h is associated with the strongest and deepest convection located at what is now the northern end of the convective line. The inflow, if elevated, may help produce deeper lifting at the cold-pool edge leading to more erect, stronger convection (Weisman 1992). As in the no-Coriolis case, there are regions in the line where the rear inflow descends to the surface and enhances low-level convergence along the gust front. Again, however, we believe that the rear-inflow dynamics is of secondary importance in driving the line evolution (system propagation to the south, with convection enhanced to the south and repressed to the north of line center) because the rear inflow forms as a result of and after the convective enhancement.

5. MCV formation

At early times in the Coriolis simulation, the convergence of earth's vorticity enhances the positive midlevel vorticity in the northern section of the line, whereas the negative vorticity on the southern section is repressed. Figure 19 is a plot of the vorticity at 6 h for the asymmetric line and can be compared with Fig. 8 for the symmetric line. While the maximum vorticities are comparable, a significantly broader region of positive vorticity exists in the northern rear section of the line and a smaller region of negative vorticity in the south, in the case with Coriolis effects.

On the system scale, this convergence of earth's vorticity is substantial. This can be qualitatively appreciated by examining Fig. 12b, the midlevel flow field at 4 h. Strong convergence is found along the entire line. At later times, the magnitude of the convergence is not easily observed given the strong cyclonic, rather than convergent, appearance of the flow (see Fig. 14b). To examine the contribution of the convergence of earth's vorticity to the MCV scale vorticity, we have calculated the relative circulation about a material circuit enclosing the MCV at midlevels. Defining the relative circulation as

$$\Gamma = \int_C \mathbf{V}\cdot\boldsymbol{\tau}ds,$$

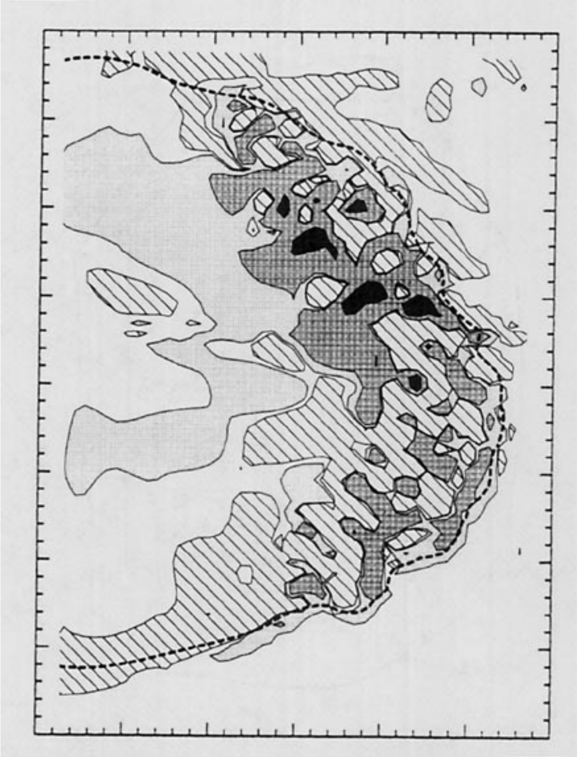

FIG. 19. Horizontal cross section of vertical vorticity at 3000 m and 6 h for the Coriolis simulation, plotted as in Fig. 8.

where C is the closed circuit, $\mathbf{V}$ is the velocity field, and $\boldsymbol{\tau}$ is a unit vector tangent to C defined such that positive circulation denotes cyclonic circulation, the time rate of change of the relative circulation, subject to the inviscid Boussinesq approximation, is

$$\begin{aligned}\frac{\partial\Gamma}{\partial t} &= \int_C B\mathbf{k}\cdot\boldsymbol{\tau}ds - f\int_C(\mathbf{V}\times\boldsymbol{\tau})ds,\\ &= \int_C B\mathbf{k}\cdot\boldsymbol{\tau}ds - f\frac{\partial A}{\partial t},\end{aligned}\qquad(2)$$

where B is the buoyancy, $\mathbf{k}$ is the vertical unit vector, and A is the area of the circuit projected onto the surface. The first term on the rhs of (2) is the solenoidal term, and the second term denotes the convergence of earth's vorticity. Figure 20 shows the position of initial and final circuits computed over a time interval from 2 to 6 h using data stored every 20 minutes from the model simulation. The circuit at 6 h lies at $z = 3$ km and the 2-h circuit lies within a kilometer above or below this level. The midlevel convergence is apparent and, as revealed in the rightmost term in (2), leads to a net increase in circulation. Figure 21 displays the time evolution of the convergence term and the relative circulation. The convergence of earth's vorticity, that is, the average system-scale convergence, remains relatively constant over time; thus, convergence is maintained as the cyclonic circulation strengthens. The

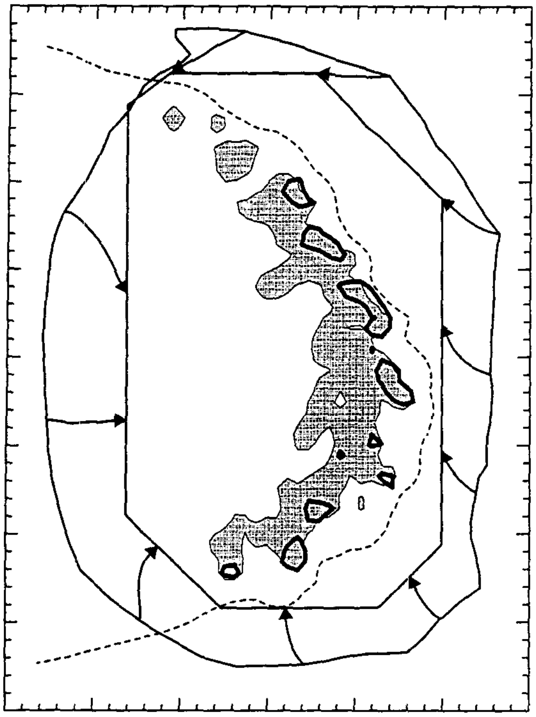

FIG. 20. Initial (2 h) and final (6 h) circuits used in the circulation calculation superposed on the midlevel vertical velocity and rainwater field (from Fig. 12b). Some trajectories are also plotted.

buoyancy contribution is found to be small, typically two orders of magnitude smaller than the convergence term. The difference between the change in the circulation and the time integral of the convergence term arises primarily from the temporal approximation of using 20-minute data and from ignoring mixing effects. The average vorticity on a surface bounded by the circuits, that is, the circulation divided by the surface area, is increasing and circulation calculations agree qualitatively with the observed MCV-scale vorticity fields in that the 6-h average vorticity value of $0.5f$ appears reasonable compared with the vorticity field at 6 h (Fig. 19).

The linear addition of vorticity from the convergence of f and that generated through line end effects, discussed in section 2c, does not completely explain the formation of the balanced vortex depicted in Fig. 15. The MCV is coincident with a midlevel mesolow, which itself is coincident with an upper-level positive buoyancy anomaly, both being found well to the north of line center. This asymmetry in the pressure and buoyancy fields is illustrated in Figs. 22a and 22b, horizontal cross sections of the midlevel pressure and buoyancy aloft at 6 and 10 h. To understand why a balanced vortex ultimately forms in the northern section of the system, an explanation is also needed for the asymmetric development of the mesolow and the upper-level buoyancy anomaly in the northern part of the system. In particular, we seek an explanation for the asymmetric nature of the positive buoyancy anomaly aloft because, given the hydrostatic nature of the flow behind the region of active convection, a positive buoyancy anomaly at upper levels implies lowered pressure beneath the anomaly.

We have identified three factors leading to the asymmetric upper-level buoyancy distribution. First, at early times, the buoyancy anomaly is produced by the upper-level convective outflow of positively buoyant air. This front-to-rear flow gradually turns toward the north due to the Coriolis force (compare Figs. 12c, 13c, and 14c). Second, at early and intermediate times (0–6 h), the active convection is strongest north of the southern line surge. As this surge progresses north, the stronger convection leads to stronger, more positively buoyant outflows in the northern section of the line relative to the southern section of the line. Finally, at later times, a significant component of the positive buoyancy anomaly is caused by subsidence warming of the rear inflow. This warming is greatest in the northern section of the system because most of this rear-to-front flow approaches from the north and the west. Thus, while Coriolis effects and the convergence of earth's vorticity are crucial to MCV formation, the overall mesoscale flow and the interaction between that flow and the convection play an equally important role in the formation of a balanced vortex. Convergence amplifies the vortex, but it is the upper-level buoyancy anomaly and its associated midlevel mesolow that determine the location of the vortex.

Examination of Fig. 15a reveals that a significant portion of the cold pool is coincident with the midlevel vortex, along with weak cyclonic circulation at the surface. The vertical cross section (Fig. 15) shows that the mesolow extends to the surface, though it is weaker at

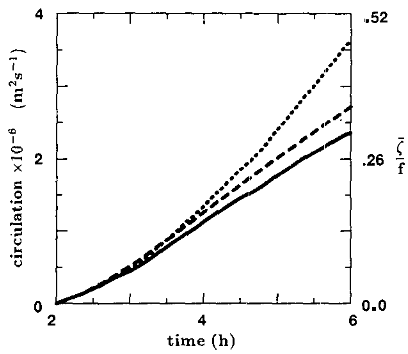

FIG. 21. The time evolution of the circulation minus the initial circulation (solid line), the average vorticity in the region enclosed by the circuit (dotted line), and the time integral of the convergence term (dashed line) from the circulation calculation. The average vorticity, with a scale given on the right axis, also denotes the average vorticity times the initial area (A_o = 77 220 km^2), with the scale given on the left axis. Thus, the average vorticity has increased due to an increase in circulation and also due to a decrease in the area enclosed by the circuit.

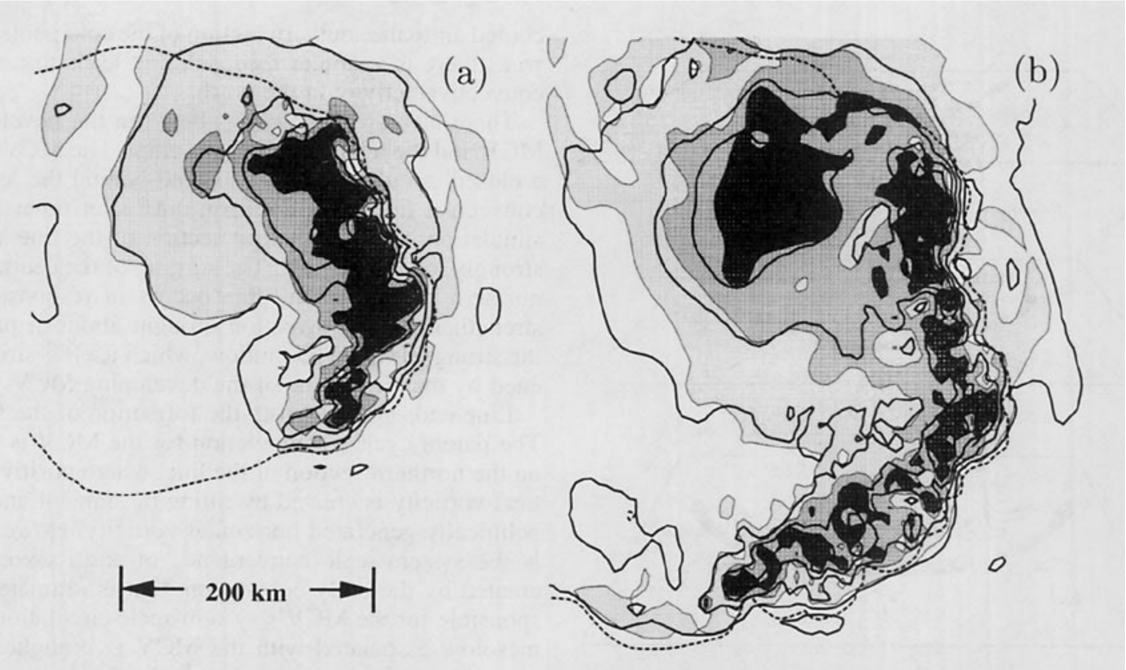

FIG. 22. Buoyancy at 5.6 km and perturbation pressure at 3 km at (a) 6 h and (b) 10 h in the Coriolis simulation. Perturbation pressure is contoured with an increment of 0.4 mb and the buoyancy is stippled with light-to-dark stippling indicating greater than (a) 0.03, 0.05, and 0.07 m s^{-2}, and (b) 0.05, 0.07, and 0.09 m s^{-2}.

the surface than aloft. The air constituting the cold pool beneath the mesolow is largely that generated in early stages of convection. It spreads out less rapidly than the air in the southern section of the cold pool due to its increasingly cyclonic flow, and its apparent location in the northern section of the mature MCS is a result of MCS growth to the south.

There is significant small-scale structure in the MCV. Figure 16 reveals that peak vorticities in the MCV are O(10f) with much higher values occurring in convectively active regions. The tilting of horizontal vorticity by processes similar to those identified in the no-Coriolis simulation and the stretching of vertical vorticity play a major role in the production of the strong vertical vorticity maxima, though the processes do not always act in unison. The higher values of vorticity are produced by convective and mesoscale processes that do not depend on Coriolis forcing and, therefore, are observed in the simulation without Coriolis effects.

6. Summary

Two squall line simulations, in an environment characterized by shallow weak shear and an absence of larger-scale forcing, are analyzed in detail. The squall lines are finite in length, as opposed to the infinitely long quasi-2D lines simulated in past studies, and the simulations document important line end effects.

In the simulation without Coriolis effects, the convective line follows the downshear-to-upshear tilting system evolution illuminated in previous 2D and 3D studies. In addition, the line ends are found to be responsible for convective evolution leading to a centralized line of strong convection and trailing flanks of weaker convection, along with a strong, centrally focused rear inflow. Line evolution is found to be largely dependent on cold pool expansion. At early times the end cells, being more three-dimensional, are more intense. They produce deeper, stronger cold pools. As these pools expand and surge relative to the pools produced by interior cells, they promote stronger convergence and lifting where they intersect with cold pools generated by interior cells. Thus, the stronger cells and the strongest line surges move toward, and ultimately reside near, the line center.

The mature system, conceptually depicted in Fig. 23, shows the strongest convection located in the central region of the line, and also depicts the flanking lines of weaker convection. At midlevels, cyclonic and anticyclonic circulation is apparent and is associated with a focusing of the rear inflow into the central portion of the leading-line convection. Both anticyclonic and cyclonic circulations arise in the outflow regions aloft. When Coriolis effects are included, the line departs from this symmetric state by 6 h. However, the mature state depicted for the no-Coriolis case is not merely of academic interest. In simulations beginning with different initial line lengths, we have found that, for a sufficiently short initial line (<100 km), the system evolves to a symmetric state quickly (~2–3 h) and Coriolis effects do not have sufficient time to promote

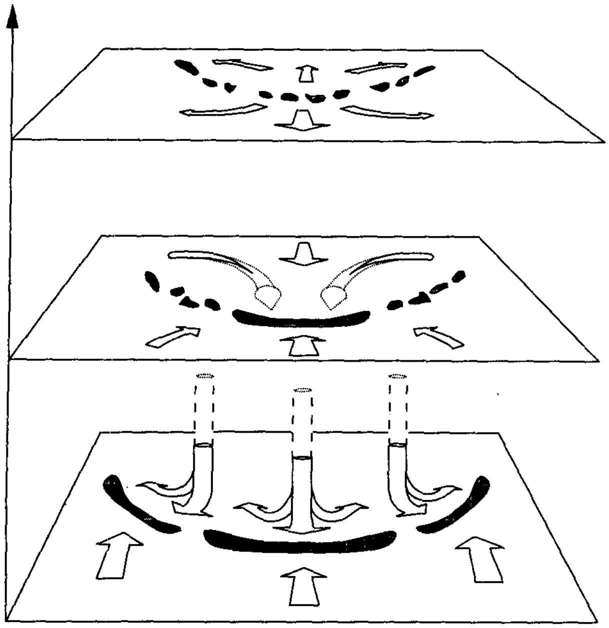

FIG. 23. Conceptual model of the mature line that has evolved without Coriolis forcing. The view is looking down from the east. The planes represent surface, mid-, and upper-level cross sections. 2D arrows denote flow in the plane and 3D tubes denote flow out of the plane. The dotted tubes depicted descending flow. The dark stippling denotes regions of updrafts and active convection.

significant line asymmetry. In this case the earlier state depicting two separate line surges often is not observed.

In comparisons with previously simulated 2D lines, the fully 3D lines possess stronger leading-line convection. Thus, 2D theory may underpredict the robustness of developing MCSs. The line ends of the fully 3D lines are also found to be responsible for some observed line asymmetries; in the mature system, the convection in the central portion of the line is stronger than the convection found on the line flanks.

In the simulation where Coriolis effects are included, the line evolves into a system that bears strong resemblance to certain observed asymmetric MCSs and MCCs. This system, conceptually depicted in Fig. 24, possesses strong anticyclonic outflow aloft, a midlevel MCV, and strong divergent flow behind the convective line at the surface, as is often observed. The mature simulated system is also found to propagate to the right of the mean low-level shear vector, as is often the case for observed systems.

Significant interactions between the convection and the system-scale circulation are found. The system-scale circulation, particularly the cold pool expansion in the presence of Coriolis forcing, enhances the convective forcing in the central and southeastern portions of the line while reducing convective forcing on the northern flank of the line. The enhanced convection provides a positive feedback to the cold pool as it expands to the south by providing more evaporatively cooled air to the southern section of the cold pool. Likewise, there is a similar feedback that leads to reduced convective activity in the north.

There also are interactions between the developing MCV and the leading-line convection. The MCV, with a closed circulation center located behind the leading convective line, does not form until later times in the simulation, after the central section of the line surges strongly toward the east. The surging of the central and northern portion of the line occurs in response to a strengthening of convection brought about in part by the strong, elevated rear inflow, which itself is strengthened by the circulation of the developing MCV.

Line ends are crucial to the formation of the MCV. The parent cyclonic circulation for the MCV is found on the northern section of the line, where positive vertical vorticity is created by tilting of ambient and baroclinically generated horizontal vorticity. However, it is the system-scale convergence of earth's vorticity, created by the early convection, that is ultimately responsible for the MCV's system-scale circulation. The mesolow associated with the MCV is brought about primarily by the presence of a positive buoyancy anomaly above it. This anomaly forms in the northern rear portion of the system in part because the outflow aloft turns to the north in response to the Coriolis forcing. The anomaly is also augmented at later times by subsidence warming in the northwesterly descending rear inflow.

Frequently observed MCV features are found in the simulated mature MCV circulation. As is shown, Coriolis forcing is crucial to the formation of an MCV with

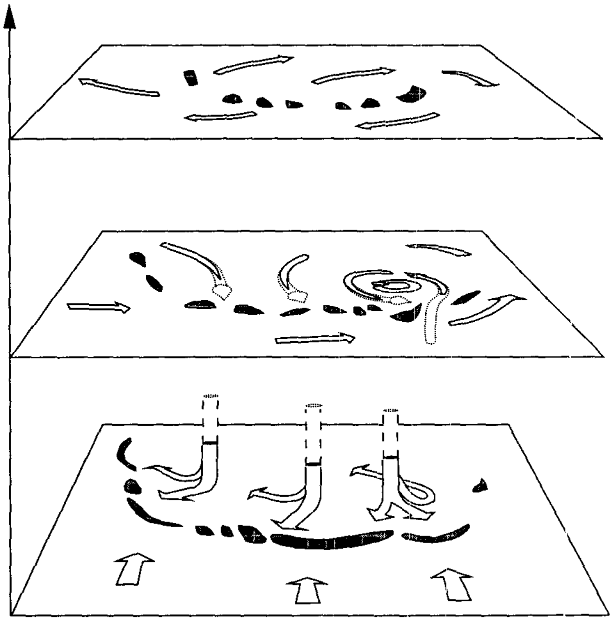

FIG. 24. Conceptual model of the mature line that has evolved with Coriolis forcing, rendered as in Fig. 23.

a closed circulation separated from the convective line, with the large-scale cyclonic circulation driven primarily by the convergence of earth's vorticity. The maximum vorticity in the mature MCV approaches $10f$, but this strong vorticity is limited in scale and is produced primarily through localized tilting and stretching of horizontal vorticity. This region of large vorticity is found between the ascending front-to-rear and descending rear-to-front flow. The MCV also has significant small-scale structure. At early times, before the development of the main MCV, smaller-scale vortices are found that are similar to those that are noted in observations. These convective-scale vortices, with vorticity approaching $100f$, are found in the vicinity of the MCV and are associated with active or decaying convection. Finally, the MCV has been produced in an environment with no large-scale forcing. In particular, there is no ambient relative vertical vorticity in the environment. For tropical systems, Schubert and Hack (1982) and Schubert et al. (1980) have suggested that preexisting relative vorticity is important in the development of an inertially stable vortex, and Bartels and Maddox (1991) suggest that this may also be important for midlatitude systems.

The Coriolis simulation shows that realistic MCSs, with significant large-scale circulations, can develop in the absence of any large-scale forcing and also in the absence of horizontal inhomogeneities in the environment. If horizontal inhomogeneities were to be included in the environment—in particular, if the base state were to be in thermal wind balance with everything else remaining unchanged—the convective instability would be enhanced to the south and decreased to the north of the line center. Thus, the expected effect on convection would be similar to what is observed in the simulation; the convection would be enhanced to the south and repressed to the north with resulting line growth and progression to the south. While system growth on the south may occur because of increasing instability to the south due to a preexisting thermal wind balance, and while this may often be augmented by the observed climatology where low-level moisture increases to the south in the central Great Plains, we have demonstrated that these factors are not the only causes, and in many cases may not even be the primary causes, of southward system propagation.

REFERENCES

Bartels, D. L., and R. A. Maddox, 1991: Midlevel cyclonic vortices generated by mesoscale convective complexes. *Mon. Wea. Rev.*, **119**, 104–118.

Biggerstaff, M. I., and R. A. Houze, 1991: Midlevel vorticity structure of the 10–11 June 1985 squall line. *Mon. Wea. Rev.*, **119**, 3066–3079.

Bjerknes, J., 1935: Saturated-adiabatic ascent of air through dry adiabatically descending environment. *Quart. J. Roy. Meteor. Soc.*, **64**, 325–330.

Brandes, A. E., 1990: Evolution and structure of the 6–7 May 1985 mesoscale convective system and associated mesovortex. *Mon. Wea. Rev.*, **118**, 109–127.

——, and C. L. Ziegler, 1993: Mesoscale downdraft influences on vertical vorticity in a mature mesoscale convective system. *Mon. Wea. Rev.*, **121**, 1337–1353.

Brown, R. A., 1970: A secondary flow model for the planetary boundary layer. *J. Atmos. Sci.*, **27**, 742–757.

Davis, C. A., and M. L. Weisman, 1994: Balanced dynamics of simulated, long-lived, mesoscale convective systems. *J. Atmos. Sci.*, 2005–2030.

Droegemeier, K. K., and R. B. Wilhelmson, 1985: Three-dimensional numerical modeling of convection produced by interacting thunderstorm outflows. Part I: Control simulation and low-level moisture variations. *J. Atmos. Sci.*, **42**, 2381–2403.

Fovell, R. G., 1991: Influence of the Coriolis force on two-dimensional model storms. *Mon. Wea. Rev.*, **119**, 606–630.

——, and Y. Ogura, 1989: Effect of vertical wind shear on numerically simulated multicell storm structure. *J. Atmos. Sci.*, **46**, 3144–3176.

Houze, R. A., S. A. Rutledge, M. I. Biggerstaff, and B. F. Smull, 1989: Interpretation of Doppler weather radar displays of midlatitude mesoscale convective systems. *Bull. Amer. Meteor. Soc.*, **70**, 608–619.

——, B. F. Smull, and P. Dodge, 1990: Mesoscale organization of springtime rainstorms in Oklahoma. *Mon. Wea. Rev.*, **118**, 613–654.

Johnson, R. H., and D. L. Bartels, 1992: Circulations associated with a mature-to-decaying midlatitude mesoscale convective system. Part II: Upper-level features. *Mon. Wea. Rev.*, **120**, 1301–1320.

Johnston, E. C., 1981: Meso-scale vorticity centers induced by mesoscale convective complexes. M.S. thesis, Department of Meteorology, University of Wisconsin—Madison, 54 pp.

Klemp, J. B., and R. B. Wilhelmson, 1978: The simulation of three-dimensional convective storm dynamics. *J. Atmos. Sci.*, **35**, 1070–1096.

Lafore, J., and M. W. Moncrieff, 1989: A numerical investigation of the organization and interaction of the convective and stratiform regions of tropical squall lines. *J. Atmos. Sci.*, **46**, 521–544.

Leary, C. A., and E. N. Rappaport, 1987: The life cycle and internal structure of a mesoscale convective complex. *Mon. Wea. Rev.*, **115**, 1503–1527.

Maddox, R. A., 1980: Mesoscale convective complexes. *Bull. Amer. Meteor. Soc.*, **61**, 1374–1387.

——, 1983: Large scale meteorological conditions associated with midlatitude, mesoscale convective complexes. *Mon. Wea. Rev.*, **111**, 1475–1495.

Menard, R. D., and J. M. Fritsch, 1989: A mesoscale convective complex-generated inertially stable warm core vortex. *Mon. Wea. Rev.*, **117**, 1237–1261.

Miller, P. P., and D. R. Durran, 1991: On the sensitivity of downslope windstorms to the asymmetry of the mountain profile. *J. Atmos. Sci.*, **48**, 1457–1473.

Raymond, D. J., and H. Jiang, 1990: A theory for long-lived mesoscale convective systems. *J. Atmos. Sci.*, **47**, 3067–3077.

Rotunno, R., J. B. Klemp, and M. L. Weisman, 1988: A theory for strong, long-lived squall lines. *J. Atmos. Sci.*, **45**, 463–485.

Skamarock, W. C., and J. B. Klemp, 1993: Adaptive grid refinement for two-dimensional and three-dimensional nonhydrostatic atmospheric flow. *Mon. Wea. Rev.*, **121**, 788–804.

Schubert, W. H., and J. J. Hack, 1982: Inertial stability and tropical cyclone development. *J. Atmos. Sci.*, **39**, 1687–1697.

——, ——, P. L. Silva Dias, and S. R. Fulton, 1980: Geostrophic adjustment in an axisymmetric vortex. *J. Atmos. Sci.*, **37**, 1464–1484.

Stirling, J., and R. M. Wakimoto, 1989: Mesoscale vortices in the stratiform region of a decaying midlatitude squall line. *Mon. Wea. Rev.*, **117**, 452–458.

Velasco, I., and J. M. Fritsch, 1987: Mesoscale convective complexes in the Americas. *J. Geophys. Res.*, **92**, 9519–9613.

Verlinde, J., and W. R. Cotton, 1990: A mesoscale vortex couplet observed in the trailing anvil of a multicellular convective complex. *Mon. Wea. Rev.*, **118**, 993–1010.

Weisman, M. L., 1992: The role of convectively generated rear-inflow jets in the evolution of long-lived mesoconvective systems. *J. Atmos. Sci.*, **49,** 1826–1847.

——, 1993: The genesis of long-lived bow echoes. *J. Atmos. Sci.*, **50,** 645–670.

——, and J. B. Klemp, 1982: The dependence of numerically simulated convective storms on vertical wind shear and buoyancy. *Mon. Wea. Rev.*, **110,** 504–520.

——, and R. Rotunno, 1988: Structure and evolution of numerically simulated squall lines. *J. Atmos. Sci.*, **45,** 1990–2013.

Zhang, D. L., 1992: The formation of a cooling-induced mesovortex in the trailing stratiform region of a midlatitude squall line. *Mon. Wea. Rev.*, **120,** 2763–2785.

——, and J. M. Fritsch, 1987: Numerical simulation of the meso-β scale structure and evolution of the 1977 Johnstown flood. Part II: Inertially stable warm-core vortex and the mesoscale convective complex. *J. Atmos. Sci.*, **44,** 2593–2612.

——, and ——, 1988a: A numerical investigation of a convectively generated, inertially stable, extratropical warm-core mesovortex over land. Part I: Structure and evolution. *Mon. Wea. Rev.*, **116,** 2660–2687.

——, and ——, 1988b: Numerical sensitivity experiments of varying model physics on the structure, evolution and dynamics of two mesoscale convective systems. *J. Atmos. Sci.*, **45,** 261–293.

——, E. Y. Hsie, and M. W. Moncrieff, 1988: A comparison of explicit and implicit predictions of convective and stratiform precipitating weather systems with a meso-β-scale numerical model. *Quart. J. Roy. Meteor. Soc.*, **114,** 31–60.

——, K. Gao, and D. B. Parsons, 1989: Numerical simulation of an intense squall line during the 10–11 June 1985 PRE-STORM. Part I: Structure and evolution. *Mon. Wea. Rev.*, **117,** 960–994.